Revision N°1

Quantification of excess ^{231}Pa in late Quaternary igneous baddeleyite

Word count: 7324.

Yi Sun[1,*,a], Axel K. Schmitt[1], Lucia Pappalardo[2], Massimo Russo[2]

[1]Institute of Earth Sciences, Heidelberg University, Im Neuenheimer Feld 236, D-69120 Heidelberg, Germany.

[2]Osservatorio Vesuviano, Istituto Nazionale di Geofisica e Vulcanologia, via Diocleziano 328, 80124 Naples, Italy.

*E-mail: yi.sun@erdw.ethz.ch

Abstract

Initial excess protactinium (^{231}Pa) is a frequently suspected source of discordance in baddeleyite (ZrO_2) geochronology, which limits accurate U/Pb dating, but such excesses have never been directly demonstrated. In this study, Pa incorporation in late Holocene baddeleyite from Somma-Vesuvius (Campanian Volcanic Province, central Italy) and Laacher See (East Eifel Volcanic Field, western Germany) was quantified by U-Th-Pa measurements using a large-geometry ion microprobe. Baddeleyite crystals isolated from subvolcanic syenites have average U concentrations of ~200 ppm and are largely stoichiometric with minor abundances of Nb, Hf, Ti, and Fe up to a few weight percent. Measured (^{231}Pa)/(^{235}U) activity ratios are significantly above the secular equilibrium value of unity and range from 3.4(8) to 14.9(2.6) in Vesuvius baddeleyite and from 3.6(9) to 8.9(1.4) in Laacher See baddeleyite (values within parentheses represent uncertainties in the last significant figures reported as 1σ throughout the text). Crystallization ages of 5.12(56) ka (Vesuvius; MSWD = 0.96, n = 12) and 15.6(2.0) ka (Laacher See; MSWD = 0.91, n = 10) were obtained from (^{230}Th)/(^{238}U) disequilibria for the same crystals, which are

[a] Present address: Institute of Geochemistry and Petrology, ETH Zürich, Clausiusstrasse 25, 8092 Zürich, Switzerland

This is the peer-reviewed, final accepted version for American Mineralogist, published by the Mineralogical Society of America.
The published version is subject to change. Cite as Authors (Year) Title. American Mineralogist, in press.
DOI: https://doi.org/10.2138/am-2020-7449. http://www.minsocam.org/

close to the respective eruption ages. Applying a corresponding age correction indicates average initial $(^{231}Pa)/(^{235}U)_0$ of 8.8(1.0) (Vesuvius) and 7.9(5) (Laacher See). For reasonable melt activities, model baddeleyite-melt distribution coefficients of D_{Pa}/D_U = 5.8(2) and 4.1(2) are obtained for Vesuvius and Laacher See, respectively. Speciation-dependent (Pa^{4+} vs. Pa^{5+}) partitioning coefficients (*D* values) from crystal lattice strain models for tetra- and pentavalent proxy ions significantly exceed D_{Pa}/D_U inferred from direct analysis of ^{231}Pa for Pa^{5+}. This is consistent with predominantly reduced Pa^{4+} in the melt, for which *D* values similar to U^{4+} are expected. Contrary to common assumptions, baddeleyite-crystallizing melts from Vesuvius and Laacher See appear to be dominated by Pa^{4+} rather than Pa^{5+}. An initial disequilibrium correction for baddeleyite geochronology using $D_{Pa}/D_U = 5 \pm 1$ is recommended for oxidized phonolitic melt compositions.

Keywords: baddeleyite, accessory mineral, Uranium series, protactinium, geochronology, trace elements

Introduction

Baddeleyite (ZrO_2) is a late-stage accessory Zr-mineral, which occurs in a wide range of silica-undersaturated, (ultra-)mafic or alkaline rocks, including carbonatites, kimberlites, metacarbonates, layered intrusions, gabbroic intrusions and plutons, dolerite dikes or alkaline syenites (Heaman and LeCheminant 1993). Extraterrestrial baddeleyite has been reported from Martian shergottite, nakhlite and chassignite (SNC) meteorites and lunar mare basalts (e.g., Heaman and LeCheminant 1993; Herd et al. 2007; Rasmussen et al. 2008). Baddeleyite usually shows high abundances of U, low diffusivity of U and Pb at magmatic temperatures, and minor to negligible incorporation of common Pb, resulting in its proliferation as a U-Pb or Pb-Pb geochronometer especially for silica undersaturated compositions (Heaman and LeCheminant 1993; Söderlund et al. 2013; Ibañez-Mejia et al. 2014). Robust U/Pb ages can be obtained with

baddeleyite, owing to its low susceptibility for secondary Pb loss (Heaman and LeCheminant 2001) and higher resistance against radiation damage (metamictization) in comparison to zircon (Heaman and LeCheminant 2001; Rioux et al. 2010; Davies et al. 2018). Furthermore, baddeleyite readily reacts with free SiO_2 during metamorphic or secondary magmatic-hydrothermal events to form secondary zircon, ruling out its presence as a metamorphic phase or xenocryst in most geological environments, thus simplifying the geological interpretation of baddeleyite ages (e.g., Davidson and Van Breemen 1988; Heaman and LeCheminant 1993; Söderlund et al. 2013).

Baddeleyite geochronology can return precise emplacement ages of mafic dike swarms, which are interpreted as the crustal pathways of flood basalts in large igneous provinces (LIPs; e.g., Fahrig 1987; Ernst and Buchan 1997; Ernst et al. 2005). Age populations of baddeleyite can then be used to define a magmatic "barcode" of a craton, where discrete sets of radiometric dates reflect the temporal sequence of regional magmatic events. This allows correlation of such events between once connected terrains, which have since been dispersed to different continents by continental rifting (e.g., Ernst et al. 2005; Söderlund et al. 2010; Reis et al. 2013; Teixeira et al. 2016; Baratoux et al. 2018). High-precision U/Pb or $^{207}Pb/^{206}Pb$ baddeleyite ages coupled with paleomagnetic data from the same lithologies are thus a powerful tool for large-scale paleographic reconstructions (e.g., Ernst and Buchan 1997; Teixeira et al. 2013; Pisarevsky et al. 2015; Baratoux et al. 2018).

One unresolved problem, however, is that baddeleyite often yields discordant ages, which are in some cases attributed to post-magmatic alteration of baddeleyite and replacement or overgrowth by zircon (Heaman and LeCheminant 1993; Rioux et al. 2010; Söderlund et al. 2013), resulting in mixed analyses between primary baddeleyite and secondary zircon rims (Rioux et al. 2010; Söderlund et al. 2013). To overcome this, multistep HCl-HF digestion techniques are

This is the peer-reviewed, final accepted version for American Mineralogist, published by the Mineralogical Society of America.
The published version is subject to change. Cite as Authors (Year) Title. American Mineralogist, in press.
DOI: https://doi.org/10.2138/am-2020-7449. http://www.minsocam.org/

applied to separate zircon and baddeleyite into different liquid fractions (Rioux et al. 2010). Other suspected sources of discordance are fast-pathway post-crystallization Pb-loss (Rioux et al. 2010; Ibañez-Mejia et al. 2014), alpha recoil losses of Pb from the outermost crystal domains (Davies and Davies 2018), or diffusive Rn loss (Heaman and LeCheminant 2001).

Another frequently conjectured possibility is that magmatic baddeleyite crystallized with a significant degree of initial excess or deficiency of ^{231}Pa and/or ^{230}Th relative to secular equilibrium in the U-series decay chains (Heaman and LeCheminant 2001; Amelin and Zaitsev 2002; Crowley and Schmitz 2009; Rioux et al. 2010; Ibañez-Mejia et al. 2014; Davies and Davies 2018). In contrast to daughter nuclide losses by recoil or diffusion processes, initial decay chain disequilibrium is mostly unaffected by grain size or shape. Thorium depletion relative to U is characteristic for baddeleyite (e.g., Wu et al., 2015), and the initial deficit in ^{230}Th can be estimated by ^{232}Th as a proxy; its effect on ^{206}Pb/^{238}U and ^{207}Pb/^{206}Pb zircon or baddeleyite ages may require disequilibrium corrections of up to ca. 100 ka that are significant for Cenozoic ages (Schmitz and Bowring 2001; Crowley et al. 2007; Ickert et al. 2015). Anomalous ^{207}Pb/^{206}Pb baddeleyite ages that are also consistently older than corresponding zircon ages, however, have been explained by the favored incorporation of ^{231}Pa into baddeleyite during crystallization (Amelin and Zaitsev 2002; Crowley and Schmitz 2009). The isotope ^{231}Pa is an intermediate daughter of ^{235}U and its in-situ decay with a half-life of 32.71 ka (Robert et al., 1969) will lead to radiogenic ^{207}Pb excesses in the mineral. An initial excess of $D_{Pa}/D_U = 10$, for example, would significantly affect ^{207}Pb/^{206}Pb ages over the entire Phanerozoic eon, considering the analytical precision of 0.1% (relative) routinely achieved by isotope dilution - thermal ionization mass spectrometry (ID-TIMS) methods (Fig. 1).

While ^{231}Pa excesses have been directly observed for Holocene and late Pleistocene zircon using secondary ionization mass spectrometry (SIMS) techniques (Schmitt 2007, 2011) and indirectly

documented for late Cenozoic zircon (e.g., Rioux et al. 2015), the partitioning of Pa relative to U has not yet been quantified for baddeleyite. This paper presents the first direct evidence for ^{231}Pa excess in baddeleyite by SIMS analysis of Holocene and late Pleistocene baddeleyite crystals from young alkaline volcanic systems of southern Italy and the Eifel (western Germany). Due to their young eruption ages (ca. 4 and 13 ka; see below), disequilibrium in (^{231}Pa)/(^{235}U) (parentheses indicate activities throughout the text) is reasonably expected. Crystallization age-corrected (^{231}Pa)/(^{235}U) ratios are used to constrain the relative partitioning coefficient D_{Pa}/D_{U} between baddeleyite and melt, which is essential for disequilibrium corrections of high-precision baddeleyite ^{207}Pb/^{206}Pb and ^{207}Pb/^{235}U ages. To further explore the partitioning behavior of Pa in magmatic minerals with respect to its speciation (Pa^{4+} or Pa^{5+}), valency-specific melt-mineral partition coefficients were modelled for baddeleyite applying crystal lattice strain theory.

Geological setting

Vesuvius

The Somma-Vesuvius (Campanian Volcanic Province, Central Italy) is a composite stratovolcano consisting of the older Somma caldera (~5 km diameter) and the younger Vesuvius cone, which formed inside the caldera following the last Plinian eruption in 79 CE (Cioni et al. 1999). Four major Plinian eruptions occurred at Somma-Vesuvius during the last 19 ka, including the Bronze Age Pomici di Avellino eruption ^{14}C-dated at 3945 ± 10 cal BP using organic material from excavated trenches (Sevink et al. 2011; throughout the text, uncertainties indicated as ± values are from the literature, or a subjective estimate of uncertainties; otherwise uncertainties are stated in parentheses as the estimated standard deviation for the last significant figures). About 50 km^3 of alkaline, ultrapotassic magma showing varying degrees of SiO_2-undersaturation have been erupted by Somma-Vesuvius (Di Renzo et al. 2007) in the ca. 25,000 years of its volcanic history.

Composition of lavas and pyroclastic rocks ranges from shoshonites, K-trachytes, K-latites and (phono-) tephrites to leucitic phonolites (Ayuso et al. 1998; Di Renzo et al. 2007). Pre-eruptive evolved magma was stored at mid-crustal depths of 8–10 km below sea level (Di Renzo et al. 2007; Scaillet et al. 2008), possibly replenished by deeper (14–16 km) tephritic magma (Pappalardo and Mastrolorenzo 2010). Magmatic temperatures range from ~1200°C for the primitive source magma to ~800°C for highly evolved phonolitic melts including those erupted during the Avellino eruption (Barberi et al. 1981; Scaillet et al. 2008). The Avellino magma was slightly oxidized with a log f_{O2} = + 1.24 relative to the Ni-NiO buffer (NNO) calculated for Avellino pumice (Marini et al. 1998).

Laacher See

The Laacher See volcano (East Eifel Volcanic Field, western Germany) is the youngest evolved volcano of the Holocene East Eifel Volcanic Field and erupted ~5.3 km^3 of compositionally zoned phonolite at 12.90 ± 56 ka BP as constrained by $^{40}Ar/^{39}Ar$ dating of sanidine phenocrysts (van den Bogaard 1995; Schmincke 2007). Erupted lithologies range from highly evolved and crystal-poor phonolite at the base of the sequence (LLST, Lower Laacher See Tephra) to mafic and crystal-rich (up to 55 %) phonolite (ULST, Upper Laacher See Tephra) at the top (Wörner and Schmincke 1984; Schmincke 2007). Fragments of cumulate and plutonic rocks include evolved syenites and carbonatites within LLST deposits (Schmitt et al. 2010b). The temperature in the most evolved portions of the LLST magma at ~5–6 km depth (Harms et al., 2004) was 720–760°C (Berndt et al. 2001). Oxidizing conditions in Laacher See magma are implied by the presence of hauyne, whose stability is favored at high f_{O2} (≈ NNO + 2.3; Berndt et al. 2001), whereas S-speciation in Laacher See phonolite glass inclusions (Harms and Schmincke 2000) suggests slightly lower fO_2 = NNO + 1 for Laacher See tephra (Harms et al. 2004).

Samples and reference materials

Sample origin and description

Two baddeleyite-rich syenite specimens from Vesuvius and Laacher See were selected for study. Both syenites are interpreted as subvolcanic, plutonic rocks crystallized from highly fractionated fluids or melts in the largely solidified roof parts of the magma chamber. Fragments of these syenites were transported to the surface by subsequent eruptions and are present as accessory lithic components in proximal tephra deposits of both volcanoes.

The Vesuvius sample (Erc-b) was collected by one of us (M. R.) and Imma Punzo (Gruppo Mineralogico Geologico Napoletano) in the San Vito Quarry (40°49′50.91′′N, 14°22′54.84′′E) near Ercolano (Campania, Italy), where proximal Avellino deposits were quarried. Subvolcanic syenites, plutonic cumulate rocks, and skarns are present as accessory lithic components in the central to upper section (stratigraphic units EU3-EU5) of the pyroclastic pumice sequence (Sulpizio et al. 2010a, 2010b). The coarse grained, holocrystalline and porous (pore volume ~20%) syenite contains sanidine as the main felsic constituent (70%). Euhedral sanidine forms tabular crystals up to 3 mm size which are intergrown in irregular orientation. Sodalite (~5%) is present as poikilitic crystals intergrown with euhedral sanidine. Mafic minerals include clinopyroxene (15%) and opaque Fe-Ti-Oxides (10%), which are subhedral and show smaller grain sizes (up to 1 mm) in comparison to alkali feldspar. Fluorcalciopyrochlore, baddeleyite, fluorite and britholite-(Ce) occur as late-stage accessory phases. These accessory phases occur as small (usually <500 μm), euhedral to subhedral crystals in the interstitial volumes between sanidine crystals (Fig. 2a). Baddeleyite forms transparent, light brown tabular crystals (<700 μm) with typical striations along the c-axis (Fig. 2a).

A second syenite sample (LS-b; Fig. 2b) was collected from LLST deposits at In den Dellen pumice quarry (50°23'39.49"N, 7°17'6.48"E) near Mendig, East Eifel Volcanic Field (Germany). The porous (10%) syenite is dominated by euhedral but heterogranular (100–3000

μm) tabular sanidine (80%) lacking any preferred orientation. Hauyne (10%) forms euhedral, isometric crystals of ~300 μm in diameter (Fig. 2c). Green pleochroic clinopyroxene (10%; 1-2 mm; Fig. 2d) and Fe-Ti oxides (up to 500 μm) are present as subhedral grains intergrown with sanidine. Accessory minerals (baddeleyite, titanite, pyrochlore) of late-stage origin occur in interstitial volumes of the feldspar as euhedral to subhedral grains (<200 μm). Laacher See baddeleyite shows a light grey color and an otherwise identical optical appearance as those from the Vesuvius samples.

Reference baddeleyite

Phalaborwa baddeleyite is an established reference material for baddeleyite U-Pb geochronology and originates from the Phalaborwa complex, a small (6 × 2.5 km) composite intrusion, which consists largely of clinopyroxenitic cumulate rocks (Reischmann et al. 1995; Heaman 2009). The grains used for study are ~100 μm in size, dark brown to black and translucent. Phalaborwa baddeleyite with a $^{207}Pb/^{206}Pb$ age of 2059.60(18) Ma is homogeneous in age despite minor (<1%) discordance (Heaman 2009). It shows homogeneity for most major and minor components; however, trace element abundances (e.g., Nb, Ta, U) are variable (Heaman 2009).

Methodology

Sample preparation

Baddeleyite grains were released from the syenite samples by gentle grinding with an agate mortar, hand-picked, and embedded in Struers CaldoFix epoxy together with grains of Phalaborwa reference baddeleyite. The mount was ground with silicon carbide paper (grain size 5 μm) and polished with diamond polishing paste (grain size 0.25 μm). Samples were cleaned in an ultrasonic bath with a three-step cleaning routine using ammoniacal EDTA solution, demineralized water and methanol to remove contaminants from the sample surface. Prior to the analyses, conductive Au coatings of 10 nm (for electron microscopy) and 50 nm thickness (for

SIMS) were applied on the epoxy mount. For Raman spectroscopy, the Au coating was removed by re-polishing with diamond polishing paste. Carbon coating was carried out on the samples prior to semiquantitative energy-dispersive X-ray spectroscopy (EDS) at the scanning electron microscope.

Electron microscopy and Raman spectroscopy

Electron microscopy was employed to image internal structures and provide semi-quantitative major component analyses of Vesuvius and Laacher See baddeleyite crystals. Back-scattered electron (BSE) imaging was performed using a Zeiss Evo MA15 instrument equipped with an Oxford instruments X-Max^{N} 150 mm^2 energy-dispersive X-ray detector to identify chemical zonation, intergrowths, signs of alteration and fractures. The same instrument was subsequently utilized for chemical analyses by EDS at high sensitivity. Semi-quantitative EDS analyses of major and minor elements were conducted after the ion probe measurements to avoid contamination from the conductive carbon coating necessary for EDS. Additional mineralogical characterizations of inclusions and host phases were performed by Raman spectroscopy using an WITec Alpha 300R Raman microscope with a UHTS300S spectrometer and a laser source wavelength of 532 nm.

SIMS measurements

Measurements of U-Th-Pa isotopes and trace element concentrations were carried out using a large-geometry CAMECA 1280-HR instrument.

U-Th-Pa excess and disequilibrium dating.

Uranium, Th and Pa isotopes were measured in baddeleyite to quantify ^{231}Pa excesses and to obtain ^{238}U/^{230}Th isochron ages. A mass-filtered $^{16}O^-$ primary ion beam was accelerated at -13 kV and tuned by apertures and electrostatic lenses to a probe current of ~60 nA at the sample surface

and a lateral spot diameter of 30–40 μm. Secondary ions were extracted at +10 kV with an energy bandpass of 50 eV and presputtering (60 s) was enabled to remove the conductive Au coating.

All actinides including Pa were measured as their respective oxide species (e.g., $^{231}Pa^{16}O^{+}$) due to their higher production rate in comparison to the atomic species of the same elements. Oxygen-flooding (~1.3×10^{-3} Pa as measured by the sample chamber vacuum gauge) was enabled to further increase oxide production rates, resulting in higher yields of secondary oxide ions and thus higher measured intensities (e.g., Schuhmacher et al. 1993; Schmitt et al. 2010a). The following species were measured (O refers to the isotope ^{16}O throughout the paragraph): $^{90}Zr_2O_4$, $^{90}Zr^{92}ZrO_4$, ^{230}ThO, $^{91}Zr^{92}ZrO_4$, ^{231}PaO, ^{232}ThO, ^{235}UO, ^{238}UO. For the unknowns, 50 magnetic cycles were measured (100 cycles for the reference material) and counting times were adjusted to values between 0.5 and 10 s in accordance to the expected intensity of the respective species. The most abundant species ^{238}UO, showing measured intensities $>10^6$ counts/s, was detected by a Faraday Cup (FC), whereas the remaining species (measured intensities $<10^6$ counts/s) were counted with an axial electron multiplier (EM). A background correction was applied for the FC detector, and the gain factor for relative sensitivity correction between FC and EM detectors was calibrated on the species ^{180}HfO in Vesuvius baddeleyite. High mass resolving power ($M/\Delta M$) of ~6000 was required to resolve all relevant isobaric interferences, which were caused by Au- or REE-bearing oxide species that were identified with the in-house Interference Calculator (Chris Coath, University of Bristol). Aside from its low concentrations in natural samples, SIMS analysis of Pa in natural minerals is typically challenged by the presence of an intense $^{232}ThO^{+}$ peak within one mass unit of the measured $^{231}PaO^{+}$ peak, even at a low abundance sensitivity of ~250 ppb (Schmitt, 2007). This leads to an elevated background at the higher mass side of the latter. In order to minimize this influence, a background subtraction was done by measuring intensities at both sides (masses 246.975 and 247.1) of the $^{231}PaO^{+}$ peak.

This is the peer-reviewed, final accepted version for American Mineralogist, published by the Mineralogical Society of America.
The published version is subject to change. Cite as Authors (Year) Title. American Mineralogist, in press.
DOI: https://doi.org/10.2138/am-2020-7449. http://www.minsocam.org/

Contributions of background relative to the measured signal range from 4 to 51% for all samples and show average values of 24% and 28% for Vesuvius and Laacher See baddeleyite, respectively.

Instrument-specific relative sensitivity for Th/U species was calibrated on secular equilibrium Phalaborwa reference baddeleyite (Wu et al. 2015) by plotting (^{230}Th)/(^{232}Th) vs. (^{238}U)/(^{232}Th); linear regression then yielded a relative sensitivity factor (RSF) of 1.15(1) (MSWD = 0.02, n = 3), similar to that in Wu et al. (2015). Relative sensitivity calibration for Pa/U was performed by measuring (^{231}Pa)/(^{235}U) ratios in Phalaborwa baddeleyite. As Phalaborwa is also expected to be in secular equilibrium for the ^{231}Pa-^{235}U system considering the shorter half-life of ^{231}Pa relative to ^{230}Th, its true (^{231}Pa)/(^{235}U) ratio can be reasonably inferred as unity. A weighted mean RSF value of 1.90(20) was obtained from averaging Phalaborwa (^{231}Pa)/(^{235}U) measured in replicate (MSWD = 1.08, n = 3); each analysis of Phalaborwa comprised 100 cycles with 50 s duration each (total duration per analysis ca. 1.5 hours) to accumulate a statistically robust number of total counts.

Trace element concentrations.

Baddeleyite domains adjacent to the U-Th-Pa spots were targeted with a mass-filtered $^{16}O^-$ primary beam (lateral spot diameter of ~20 µm) accelerated at -13 kV and secondary ions were detected in energy-filtering mode using an extraction voltage of +9.9 kV while the mass spectrometer is tuned for admission of 10 keV secondary ions with an energy bandpass of 50 eV to suppress molecular interferences. The conductive Au coating was removed by presputtering (30 s). The following elemental species were detected in monocollection mode using the axial EM at low mass resolving power M/ΔM of ~1800 (major oxide interferences stated in brackets): ^{26}Mg, ^{30}Si, ^{31}P, ^{49}Ti, ^{55}Mn, ^{57}Fe, ^{177}Hf^{2+}, ^{89}Y, ^{96}Zr, ^{139}La, ^{140}Ce, ^{141}Pr, ^{143}Nd, ^{149}Sm, ^{151}Eu, ^{158}Gd (^{142}CeO, ^{142}NdO), ^{159}Tb (^{143}NdO), ^{161}Dy (^{145}NdO), ^{165}Ho (^{149}SmO), ^{168}Er (^{152}SmO), ^{169}Tm

(^{153}EuO), ^{172}Yb (^{156}GdO), ^{175}Lu (^{159}TbO), ^{178}Hf (^{162}DyO), ^{232}Th, ^{238}U. The species ^{178}Hf (for REE, Th, U) and ^{96}Zr (for the remaining species) were used as reference masses. Five magnetic cycles were run during each analysis and counting times were adjusted to values between 1 and 12 s considering the abundance of the measured element. Although the transmission of most interference-causing oxide species can be effectively suppressed with energy filtering, significant interferences caused by oxides of light rare earth elements (LREE; here defined as La-Sm) or middle REE (MREE; Eu-Dy) were still encountered for heavier REE. These interferences were corrected by peak stripping using oxide production rates for LREE and MREE determined on doped, interference-free REE reference glasses based on Drake and Weill (1972).

Isobaric interferences by hydrides, monoatomic or polyatomic cations ineliminable by energy filtering occur for the sole (or vastly predominant) stable isotopes of Sc, Nb, and Ta: ^{45}Sc ($^{90}Zr^{2+}$), ^{93}Nb (^{92}ZrH), ^{181}Ta ($^{90}Zr^{91}$Zr). Separate analytical protocols, utilizing a very high mass resolution of ~20,000, were therefore required. Where possible, static multi-collection with a nuclear magnetic resonance (NMR) probe to stabilize the secondary magnetic field was applied. Scandium was measured in peak-hopping mode with the species $^{90}Zr^{2+}$, ^{45}Sc, ^{48}Ti and $^{96}Zr^{2+}$ being counted by an axial EM, whereas the reference mass ^{91}Zr was detected with an FC detector. Analyses were executed using 10 magnetic cycles and counting times of 2 to 6 s. Niobium (^{93}Nb) was analyzed in static multi-collection with ^{90}Zr (reference mass) and ^{93}Nb measured on FC and EM detectors, respectively, integrating over 15 4-s-counting cycles. Tantalum was detected in monocollection mode with an axial EM using peak-hopping. Counting times varied between 6 s for ^{181}Ta and 2 s for the reference mass $^{90}Zr^{2+}$.

The possibility of hydride contribution (^{180}HfH) to the measured ^{181}Ta peak, which is not resolvable even at high mass resolution, was assessed by monitoring ^{178}Hf/^{179}Hf ratios during the analyses. A ^{178}Hf/^{179}Hf ratio of ~2 is expected for natural abundances of Hf, whereas deviating

ratios would indicate the presence of Hf hydrides. Replicate measurements of $^{178}Hf/^{179}Hf$ in all baddeleyite samples, however, yielded values close to 2, and hence the presence of ^{180}HfH on Ta is deemed insignificant. Vanadium as another potential pentavalent element was considered, but counts at mass 51 were indistinguishable from EM detector noise (~0.01 counts per second).

For standardization of the measured trace element concentrations, zircon 91500 (Wiedenbeck et al. 1995; 2004) was preferred over Phalaborwa baddeleyite as the primary reference due to greater degree of chemical variation in the latter (Heaman 2009). However, Phalaborwa baddeleyite was used as a secondary reference to assess potential bias due to the matrix difference between zircon and baddeleyite. Madagascan Green zircon (MAD-559; Coble et al., 2018) was utilized as an additional secondary reference material for Sc, Nb, and Ta measurements. Stochiometric Zr abundances for zircon and baddeleyite were applied for quantification; REE anomalies were calculated as Ce/Ce* and Eu/Eu* where * indicates the geometric means from the chondrite-normalized abundances of adjacent elements (e.g., Kato et al. 2006).

Results

Mineralogical and geochemical characterization

Phalaborwa reference baddeleyite crystals contain as major non-stochiometric constituents Hf (1.08–1.50 wt%), Ti (604–1469 ppm), Nb (560–2725 ppm), U (313–1655 ppm) and Ta (81–276 ppm) with average Hf/Ti of 13.2, which is slightly higher than the value of 11.0 ± 1.7 reported by Reischmann et al. (1995). Scandium is present at average concentrations of ~100 ppm. Thorium and REE were detected in traces at concentrations <30 ppm. Chondrite-normalized REE patterns (using recommended CI chondrite abundances by McDonough and Sun 1995) show REE enrichment by a factor 10 relative to CI chondrite and minor depletion in light REE (Fig. 3a). Ranges of measured concentrations overlap with published data of Phalaborwa reference

baddeleyite by Xie et al. (2008) and Heaman (2009) for most REE, attesting to the robustness of the RSF calibration using zircon as a primary reference material. La and Pr concentrations determined in this study are significantly lower than reported in the literature, but nonetheless consistent with the expected low abundance of LREE in baddeleyite. Whereas clear Eu anomalies are absent in Phalaborwa baddeleyite (average Eu/Eu* = 1.2), it shows significant positive Ce anomalies of 30–47.

Vesuvius and Laacher See baddeleyite grains are 150-400 μm in size and appear largely homogenous in BSE images, except for slight banding in some grains that is visible as a BSE contrast. Few grains show intergrowths with associated phases, including potassic feldspar, pyrochlore and titanite. Inclusions and primary cracks, however, are largely absent and overgrowths by secondary zircon were not encountered. Vesuvius and Laacher See baddeleyite crystals are ~95 wt% ZrO_2 and contain Nb (3.37–4.66 wt% Nb_2O_5), Hf (0.50–1.78 wt% HfO_2), Ti (0.10–0.45 wt% TiO_2) as well as Fe (0.06–0.32 wt% FeO) as the main non-stochiometric components. Other trace components (Al, Mn, Ta, Mg, U) and, in Laacher See baddeleyite, also HREE are present at levels of a few 100 ppm. Whereas both Vesuvius and Laacher See baddeleyite crystals show average U concentrations of ~200 ppm, their Th abundances are on average lower by two orders of magnitude with a maximum abundance of 23.4 ppm. Baddeleyite from Vesuvius shows significantly larger variations in U (17.5–1000 ppm) in comparison to samples from Laacher See (126–468 ppm).

Chondrite-normalized REE patterns of Vesuvius baddeleyite show flat trends with $(Pr/Yb)_N$ values between 0.2 and 5.8 (Fig. 3b). Highly positive Ce anomalies with Ce/Ce* values of 6 to 421 are present and LREE, as well as HREE, are enriched in comparison to MREE by up to one order of magnitude. Eu anomalies could not be reliably determined in many samples due to Gd abundances near or below detection limit, but they are generally slightly positive

(maximum Eu/Eu* = 2). Vesuvius baddeleyite shows super-chondritic Nb/Ta ratios (50–200) and sub-chondritic $(Y/Ho)_N$ values (1–14). The Laacher See baddeleyite crystals are characterized by a prominent enrichment in HREE and chondrite-normalized REE patterns with positive slopes and $(Pr/Yb)_N$ values of 0.001 (Fig. 3c). Ce anomalies are highly positive (Ce/Ce* up to 230) and minor negative Eu anomalies are observed in some grains (minimum Eu/Eu* = 0.4). Similar to baddeleyite crystals from Vesuvius, Laacher See baddeleyite exhibit super-chondritic Nb/Ta (up to 220) and sub-chondritic $(Y/Ho)_N$ ratios (1.2–1.4).

Crystallization ages

Baddeleyite samples show strong fractionation of U against Th, resulting in high ^{238}U excesses and $(^{238}U)/(^{232}Th)$ activity ratios >>1 (Vesuvius baddeleyite 26–141; Laacher See baddeleyite 130–334), which are in a similar range for Phalaborwa reference baddeleyite ($^{238}U/^{232}Th$ activity ratios up to 328). Measured $(^{230}Th)/(^{232}Th)$ are 1.35–7.43 for Vesuvius and significantly higher for Laacher See baddeleyite (16.6–47.0).

Data points of Vesuvius and Laacher See baddeleyite crystals plot well below the equiline within a $(^{230}Th)/(^{232}Th)$ versus $(^{238}U)/(^{232}Th)$ diagram (Fig. 4a-b). Vesuvius baddeleyite analyses define an isochron corresponding to a crystallization age of 5.17(57) ka with a mean square weighted deviation (MSWD) of 0.96 (n = 12). Laacher See baddeleyite yields a U/Th isochron age of 15.5(2.0) ka with a MSWD of 0.92 (n = 10). Crystallization ages obtained from baddeleyite crystals are slightly older than published eruption ages for Avellino pumice (ca. 4 ka; Sevink et al. 2011) and the Laacher See tephra (ca. 12.9 ka BP; van den Bogaard 1995). Initial $(^{230}Th)/(^{232}Th)$ were determined from the intersections between the isochrons and the equiline, corresponding to values of 1.20(25) and -1.1(3.3) for Vesuvius and Laacher See baddeleyite, respectively. These ratios, however, are poorly constrained due to the very high $(^{238}U)/(^{232}Th)$ ratios of baddeleyite.

The above baddeleyite crystallization ages are the first to be reported for subvolcanic cumulate rocks from Somma-Vesuvius, and they indicate solidification of the upper parts of an evolved magma reservoir until briefly before eruption. Corresponding ages for Laacher See agree with those of zircon from carbonatite nodules in early erupted Laacher See tephra (Schmitt et al. 2010b). They significantly predate eruption and are suggestive of growth and differentiation of the magma reservoir a few 1000 years prior to eruption (Schmitt et al. 2010b).

Initial $(^{231}Pa)/(^{235}U)_0$ in baddeleyite

Significant $(^{231}Pa)/(^{235}U)$ excess was detected in all baddeleyite grains (Fig. 5). Vesuvius baddeleyite shows heterogenous $(^{231}Pa)/(^{235}U)$ ratios ranging from 3.4(8) to 14.9(2.6) with a weighted mean of 8.0(1.0) (MWSD = 7.37, n = 12; error here and below multiplied by square-root of MSWD to account for non-analytical scatter). Samples from Laacher See exhibit $(^{231}Pa)/(^{235}U)$ ratios from 3.6(9) to 8.9(1.4) with a weighted mean of 6.0(5) (MSWD = 2.18, n = 10). Age-correction of $(^{231}Pa)/(^{235}U)$ was performed using U/Th isochron ages obtained on the same grains and decay equations (Bateman 1910) to determine the extent of initial Pa excess at time of baddeleyite crystallization. Decay constants are taken from Cheng et al. (2013) and references therein. Average $(^{231}Pa)/(^{235}U)_0$ values are 8.8(1.0) for Vesuvius baddeleyite and 7.9(5) for Laacher See baddeleyite. These empirical values are the basis for estimating baddeleyite-melt D_{Pa}/D_U (see discussion).

Modelling of partition coefficients

Direct measurement of Pa speciation in natural baddeleyite samples from Vesuvius and Laacher See is impossible because of the very low concentrations. Hence, to explore the partitioning of reduced and oxidized Pa species into baddeleyite, D_{Pa4+} and D_{Pa5+} were modelled by applying crystal lattice strain theory (Blundy and Wood 1994; Wood and Blundy 1997). For the substitution of a trace element into a specific ion site of a host mineral M, the partition coefficient

This is the peer-reviewed, final accepted version for American Mineralogist, published by the Mineralogical Society of America.
The published version is subject to change. Cite as Authors (Year) Title. American Mineralogist, in press.
DOI: https://doi.org/10.2138/am-2020-7449. http://www.minsocam.org/

383 D can be described by the valency n, ionic radii r_0 (original ion) and r_i (substituting ion), as well
384 as elasticity of the lattice site represented by the apparent Young´s modulus of the mineral E_0,
385 following:

386 $$D_i = D_{0(M)}^{n+} * exp\left\{\frac{-4\pi N_A E_0^{n+}\left[\frac{1}{2}r_{0(M)}^{n+}\left(r_i - r_{0(M)}^{n+}\right)^2 + \frac{1}{3}\left(r_i - r_{0(M)}^{n+}\right)^3\right]}{RT}\right\}$$ (1) (Blundy and Wood 1994)

387 N_A is Avogadro´s number, T is temperature in K, and R is the universal gas constant. The
388 differences in physical properties between the substituting and the original ion will cause
389 distortions of the lattice site and build up lattice strain, lowering the partition coefficient of the
390 substituting trace element (Blundy and Wood 1994; Wood and Blundy, 1997). For homovalent
391 ions, partitioning coefficients show a near-parabolic dependency on the ionic radii for each
392 mineral (Onuma et al. 1968). Therefore, the partition coefficient of any trace element with known
393 ionic radius can be predicted, if the partitioning for a series of elements with same valency and
394 into the same mineral is well-constrained (Blundy and Wood 1994; Wood and Blundy 1997).
395 Baddeleyite-melt partition coefficients were obtained for selected trivalent (REE, Y, Sc),
396 tetravalent (Ti, Hf, U, Th), and pentavalent trace elements (Nb, Ta) using abundances determined
397 by SIMS. Corresponding trace element concentrations for the melt were approximated by the
398 compositions of the most evolved magmas of Avellino and Laacher See eruption, using glass
399 data of Avellino pumice by Tomlinson et al. (2015) and bulk-rock values for the Lower Laacher
400 See Tephra by Wörner et al. (1983). Ionic radii were taken from Shannon (1976), assuming
401 substitution of all trace elements into the same, 7-fold coordinated cation site in monoclinic
402 baddeleyite (Smith and Newkirk 1965); where ionic radii for 7-fold coordination were not
403 available, values were calculated as arithmetic averages of corresponding radii for 6-fold and 8-
404 fold coordination. Magma temperatures were constrained as 1073 K for Vesuvius and 1033 K for
405 Laacher See, based on experimental data for the uppermost magma chamber by Balcone-

Bouissard et al. (2012) and Harms et al. (2004), respectively. Partition coefficient curves (Fig. 6-7) were then modelled by least square fitting routines with orthogonal distance regression (ODR) and equation (1). For trivalent and tetravalent cations, sufficient data points were available to allow curve fitting for all three parameters D_0, E_0 and r_0. Ce was excluded from the fits, as the element is present in different oxidation states (Ce^{3+}, Ce^{4+}) under magmatic conditions. Curves for 5^+ cations were fitted for a single parameter D_0 due to the paucity of pentavalent trace elements in baddeleyite, with only Nb and Ta present at measurable concentrations. The remaining parameter r_0 was estimated from fitted values for the lower charged cations using the cation charge-dependent variations presented in Blundy and Wood (2003), and E_0 from tetravalent fit curves was used for the pentavalent partition coefficient curves. As E_0 increases with ionic charge (Blundy and Wood 2003), resulting D_0 values for 5^+ cations can be considered minimal estimations. Resulting parameters for D_0, r_0 and E_0 as indicated by the fits are presented in Table 1. Partition coefficients of Pa^{4+} and Pa^{5+} were then graphically determined considering the ionic radii of both species in 7-fold coordination (Pa^{4+} = 0.955 Å, Pa^{5+} = 0.845 Å; Shannon 1976). Respective D values for Pa^{4+} and Pa^{5+} are 4.8 ± 0.4 and 2400 ± 100 for Vesuvius baddeleyite. For Laacher See baddeleyite, D_{Pa4+} and D_{Pa5+} are 5.0 ± 0.4 and 470 ± 20, respectively. Partition coefficients were found to be similar for Pa^{4+} and U^{4+} (differences <0.5 magnitudes) in both samples. The oxidized species Pa^{5+}, however, shows a significantly higher partition coefficient in comparison to U^{4+} by approximately two orders of magnitude (Fig. 6-7). In consequence, modelled D_{Pa5+}/D_{U4+} significantly exceed empirically obtained D_{Pa}/D_U bulk partition coefficients.

Discussion

Analysis of Holocene baddeleyite indicates elevated $(^{231}Pa)/(^{235}U)_0$ at the time of crystallization. Using these data to determine D_{Pa}/D_U requires constraints on the initial $(^{231}Pa)/(^{235}U)$ of the

This is the peer-reviewed, final accepted version for American Mineralogist, published by the Mineralogical Society of America.
The published version is subject to change. Cite as Authors (Year) Title. American Mineralogist, in press.
DOI: https://doi.org/10.2138/am-2020-7449. http://www.minsocam.org/

parent melts, which are difficult to obtain for two reasons: (1) direct measurements of $(^{231}Pa)/(^{235}U)$ in Vesuvius and Laacher See rock requires handling of a radioactive Pa spike and presently, it is difficult to find a laboratory that performs these analyses for silicates on a routine basis; and (2) the intrusive syenites crystallized from highly fractionated residual fluids expelled during late-stage magmatic differentiation, and hence the bulk-rock compositions of co-erupted pumice might not be representative for the melt. Regardless of these difficulties, it is still possible to assess plausible D_{Pa}/D_U for baddeleyite-melt. For example, $(^{231}Pa)/(^{235}U)_0$ of young volcanic rocks from island and continental arcs (Huang et al. 2016, and references therein) is 1.7(4) $\times(^{231}Pa)/(^{235}U)_0$, and the corresponding factor for global compilations of recent ocean island basalts and their differentiates is 1.4(2) (Prytulak et al. 2014, and references therein). With $(^{230}Th)/(^{238}U)$ of 0.888 (protohistoric pumice; Cortini et al. 2004) and an age correction by 3.5 ka (Rolandi et al. 1998), a melt $(^{231}Pa)/(^{235}U)_0$ value of 1.51(31) was obtained for Vesuvius. For Laacher See, an age-corrected melt $(^{231}Pa)/(^{235}U)_0$ ratio of 1.90(29) was calculated using $(^{230}Th)/(^{238}U)$ of 1.022 (Lower Laacher See Tephra, glass; Schmitt et al. 2010) and an eruption age of 12.9 ka (van den Bogaard 1995). The bulk-rock composition of the most evolved Lower Laacher See tephra best approximates the highly evolved, late-magmatic fluids, from which Laacher See baddeleyite was crystallized. Using the initial zircon and melt $(^{231}Pa)/(^{235}U)_0$ values, D_{Pa}/D_U = 5.8(2) and 4.1(2) are calculated for Vesuvius and Laacher See, respectively. Uncertainties for the relation between measured $(^{230}Th)/(^{238}U)_0$ and inferred $(^{231}Pa)/(^{235}U)_0$ for melt compositions were estimated from the average residuals in fitting global compilations of volcanic rocks. This, however, is likely an underestimate because it neglects potential extremes: exceptionally high $(^{231}Pa)/(^{235}U)$ ratios were reported for lavas of Kasatochi island, Aleutian Arc, showing similar values to the highest MORB ratios (3.7; Turner et al. 2006), and mafic medieval (post-Avellino) lava from Vesuvius (up to 3.0; pers. comm. Riccardo Avanzinelli). Thus,

considering a likely range of melt $(^{231}Pa)/(^{235}U)_0$ between 1.0 and 3.0, a baddeleyite-melt $D_{Pa}/D_U = 5 \pm 1$ is proposed as a conservative estimate for melt compositions such as those represented by Vesuvius and Laacher See. Baddeleyite thus enriches Pa over U to an extent similar to, or even stronger than, zircon (~2–4; Schmitt 2007, 2011; ~2–10; Rioux et al. 2015).

The uncertainty of D_{Pa5+} modelled using crystal lattice strain theory is affected by the paucity of measurable pentavalent elements in baddeleyite, with Nb and Ta providing the only anchor points for curve fitting. We estimated uncertainties on model D_{Pa5+} considering the differences in partition coefficients for Nb and Ta. Both elements share nearly identical ionic radii and similar geochemical features, and thus, they are expected to present near-identical partition behavior in baddeleyite. Partition coefficients for Ta, however, are consistently lower in both Vesuvius and Laacher See baddeleyite compared to Nb. Curve fitting using either Nb or Ta results in likely ranges for D_0^{5+} of 570–8500 (Vesuvius) and 145–1300 (Laacher See). In spite of the variability of these values, minimum estimations are always significantly higher than the partition coefficients determined for the species Pa^{4+} (~5 in both samples), as well as bulk D_{Pa}/D_U ratios derived from SIMS U-Th-Pa measurements. The observed lower partition coefficients for Ta in comparison to Nb cannot be satisfactorily explained by the crystal lattice strain model, whereas low $D_{Th}/D_U = 0.01$ indicated by the tetravalent model parabola is fully consistent with natural baddeleyite being strongly depleted in Th relative to U (e.g., Heaman and LeCheminant 1993).

Absolute partition coefficients determined in this study may be inaccurate because of uncertainties regarding the trace element concentrations in the parent melt. While the most evolved magma composition of each eruption is used here as an approximation for melt composition, these abundances may still underestimate incompatible element enrichments in the highly fractionated residual melts of the baddeleyite-crystallizing syenites. In this case, *D* values

for incompatible elements may be overestimated. Curves for trivalent cations modelled in this study, however, bracket experimental data by Klemme and Meyer (2003) for baddeleyite in a carbonatite melt ($D_0 = 8.7 \pm 5.6$). The quality of the fitted curves is lower for LREE and progressively improves from Sm to La, reflecting the increase in compatibility for REE with higher atomic number. Tetravalent D_0 is significantly higher for both Vesuvius and Laacher See baddeleyite in comparison to the published value of 464 ± 163 by Klemme and Meyer (2003), presumably due to the different saturation conditions for baddeleyite in silicate melts vs. carbonatite melts. Moreover, Pa and U are both strongly incompatible in most rock-forming silicate minerals (Dunn and Sen 1994; LaTourrette et al. 1995; Huang et al. 2009) and thus are expected to show a similar increase in concentration during melt differentiation. Therefore, it is reasonable to assume that differences between actual and estimated concentration in the melt might be comparable for both elements, cancelling out the distortion on the relative partition coefficient D_{Pa}/D_U, even if individual partition coefficients deviate from real values.

Trace element fractionation by cogenetic phases in the syenite are a further complication, as measurements were carried out on natural baddeleyite that crystallized in a paragenesis of diverse minor and accessory phases. This fractionation effect is especially evident for REE in Vesuvius baddeleyite, where HREE/LREE ratios are much lower compared to Laacher See baddeleyite and partition coefficients for REE are also lower than experimentally obtained coefficients by Klemme and Meyer (2003). Garnet and pyrochlore are probable candidates affecting REE and other trace element abundances in these melts. Garnet has been described from Vesuvius phonolite (Scheibner et al. 2008), even though it is absent in the studied samples. The potential of garnet to deplete HREE in coexisting zircon is well established (e.g., Harley and Kelly 2007). Due to the similar partitioning behavior of baddeleyite and zircon, an equivalent effect of garnet on baddeleyite can be reasonably expected. The presence of pyrochlore in both

502 investigated syenite samples (Vesuvius and Laacher See) is petrographically confirmed, and the
503 occurrence of pyrochlore has been described for Laacher See syenite (Schmitt et al. 2010b). If
504 pyrochlore fractionated prior to baddeleyite formation, this would cause the melt to become
505 depleted in Nb and Ta (and – in decreasing degrees – Pa and U). Hence, model D values for Nb
506 and Ta (and by extrapolation Pa) using pumice data may be underestimated. The small modal
507 abundance of pyrochlore and the similarity of model D_{Pa}/D_U between Vesuvius and Laacher See
508 syenite, however, suggests that this effect is minor. Relative Ta depletion and Nb enrichment in
509 baddeleyite from subvolcanic syenites can the attributed to high-temperature fractionation
510 processes by Ti-bearing oxides (Ballouard et al. 2016). While Nb is preferentially incorporated
511 into biotite at low-temperature hydrothermal environments, Ti-bearing oxides efficiently extract
512 Ta under high-temperature pneumatolytic conditions, resulting in a relative enrichment of Nb in
513 the residual melt or fluid (Ballouard et al. 2016). This hypothesis is supported by petrographical
514 observations in both syenite samples (e.g., porous rock textures indicative of formation in
515 presence of overcritical fluids; occurrence of opaque oxide minerals).

516 Despite these potential sources of uncertainty, the expected bias resulting from them
517 appears smaller than the observed two-orders-of-magnitude discrepancy between modelled
518 D_{Pa5+}/D_{U4+} and the empirical D_{Pa}/D_U, which therefore requires a different explanation.
519 Protactinium is a redox sensitive element as shown by experiments in aqueous solutions, where it
520 is either present as Pa^{4+} or Pa^{5+} cations depending on f_{O2} (e.g., Mitsuji 1967). A predominance of
521 oxidized Pa^{5+} over Pa^{4+} under magmatic systems is widely suggested in the literature, however,
522 no direct evidence exists for this claim (cf. Huang et al. 2009). Our modelled partitioning data
523 can be reconciled with the empirical D_{Pa}/D_U from U-series analysis if the melt was dominated by
524 Pa^{4+} rather than Pa^{5+} for Vesuvius and Laacher See magmas. This is despite the fact that redox
525 conditions reported for both Vesuvius and Laacher See magma chambers are slightly more

This is the peer-reviewed, final accepted version for American Mineralogist, published by the Mineralogical Society of America.
The published version is subject to change. Cite as Authors (Year) Title. American Mineralogist, in press.
DOI: https://doi.org/10.2138/am-2020-7449. http://www.minsocam.org/

526 oxidized (by approximately two log units in f_{O2}) than typical mantle melts (e.g., Marini et al.
527 1998; Berndt et al. 2001). Both magmas are thus not anomalously reduced, which is further
528 supported by the observation of positive Ce-anomalies in baddeleyite. In contrast to common
529 assumptions, Pa^{4+} might thus be a common valence state in natural magmas. We dismiss a major
530 presence of U^{5+} and U^{6+} in evolved melts at Vesuvius and Laacher See because of the consistent
531 partitioning behavior of U with other tetravalent cations in baddeleyite (Fig. 6-7).

532 **Implications**

533 Protactinium excesses in Holocene and late Pleistocene baddeleyite indicate preferred Pa
534 baddeleyite-melt partitioning relative to U by a factor of ~5 for moderately oxidized evolved
535 alkaline magmas (log f_{O2} = NNO + 1–3) at medium to low temperatures (~800°C). Initial
536 excesses of ^{231}Pa in baddeleyite are thus equivalent to, or possibly even more severe, than for
537 zircon (Schmitt 2007; Rioux et al. 2015). These excesses require significant corrections for
538 $^{207}Pb/^{206}Pb$ and $^{207}Pb/^{235}U$ ages (Fig. 1), and hence, a correction of baddeleyite ages (e.g., Wendt
539 and Carl 1985; Ibañez-Mejia et al. 2014) is recommended using $D_{Pa}/D_U = 5 \pm 1$ (neglecting
540 potential disequilibrium in the melt phase). As the value was determined for evolved silicate
541 melts, its extrapolation to other melt compositions, especially mafic igneous or carbonatites, for
542 which baddeleyite geochronology is commonly applied, remains to be tested in future studies.
543 Comparison with partitioning of other trace elements suggests that Pa is predominantly present as
544 Pa^{4+}, even in comparatively oxidized melts. More reliable Pa disequilibrium corrections for
545 natural magmatic systems will require more robust constraints on its redox-sensitive speciation
546 and a more quantitative understanding of Pa and U partitioning into magmatic minerals.

547 The crystallization age of baddeleyite crystals, obtained here for the first time for Somma-
548 Vesuvius syenitic nodules, is also crucial for constraining magma chamber evolution before
549 major eruptions. Syenitic nodules are commonly present in association with other cumulate rocks

(e.g., pyroxenite, skarn, marble) in pyroclastic deposits of all major explosive eruptions of Vesuvius. These syenites are considered the product of magma-limestone interaction, in which skarn xenoliths represent the thermometamorphic and/or metasomatic aureole in the inner part of the interaction zone, whereas igneous rocks (syenite and clinoproxenites) are derived from the magmatic front of the outermost parts of the magma reservoir (e.g., Fulignati et al. 2004; Jolis et al. 2015 and reference therein). The timescale of this process is still unclear, although it has been recently postulated that magma-limestone interaction can be very fast and influence eruption intensities due to rapid and voluminous CO_2 release (e.g. Blythe et al. 2010). The ages presented here are inconsistent with a protracted hiatus between crystallization and eruption of the syenitic clasts, supporting the idea of a relatively rapid propagation of assimilation and crystallization front in the upper portion of the phonolitic chamber. This suggests relatively fast magma accumulation and a potential trigger mechanism for the eruption.

Acknowledgements

We are grateful to Ilona Fin and Andreas Thum (Heidelberg University) for the preparation of epoxy mounts and thin sections. The donation of samples by Imma Punzo (Gruppo Mineralogico Geologico Napoletano) is much appreciated. Alexander Varychev and Jan Schmitt (Heidelberg University) are thanked for the assistance with scanning electron microscopy and Raman spectroscopy, respectively. Riccardo Avanzinelli (University of Florence) is thanked for providing helpful information about the U-Pa systematics of Somma-Vesuvius. Journal reviewers Mauricio Ibañez-Mejia and Matt Rioux are thanked for their comprehensive and insightful comments; manuscript handling by associate editor Callum Hetherington is appreciated.

References cited

573 Amelin, Y., and Zaitsev, A. N. (2002) Precise geochronology of phoscorites and carbonatites:
574 The critical role of U-series disequilibrium in age interpretations. Geochimica et
575 Cosmochimica Acta, 66(13), 2399-2419.
576 Ayuso, R. A., De Vivo, B., Rolandi, G., Seal II, R. R., and Paone, A. (1998) Geochemical and
577 isotopic (Nd–Pb–Sr–O) variations bearing on the genesis of volcanic rocks from Vesuvius,
578 Italy. Journal of volcanology and geothermal research, 82(1-4), 53-78.
579 Balcone-Boissard, H., Boudon, G., Ucciani, G., Villemant, B., Cioni, R., Civetta, L., and Orsi, G.
580 (2012) Magma degassing and eruption dynamics of the Avellino pumice Plinian eruption
581 of Somma–Vesuvius (Italy). Comparison with the Pompeii eruption. Earth and planetary
582 science letters, 331, 257-268.
583 Ballouard, C., Poujol, M., Boulvais, P., Branquet, Y., Tartèse, R., and Vigneresse, J. L. (2016)
584 Nb-Ta fractionation in peraluminous granites: A marker of the magmatic-hydrothermal
585 transition. Geology, 44(3), 231-234.
586 Barberi, F., Bizouard, H., Clocchiatti, R., Metrich, N., Santacroce, R., and Sbrana, A. (1981) The
587 Somma-Vesuvius magma chamber: a petrological and volcanological approach. Bulletin
588 Volcanologique, 44(3), 295-315.
589 Bateman, H. (1910) The solution of a system of differential equations occurring in the theory of
590 radioactive transformations. Proceedings of the Cambridge Philosophical Society, 15,
591 423-427.
592 Blythe, L.S., Deegan, F.M., Freda, C., Jolis, E.M., Masotta, M., Misiti, V., Taddeucci, J., Troll,
593 V.R. (2015) CO_2 bubble generation and migration during magma–carbonate interaction.
594 Contributions to Mineralogy and Petrology, 169(4),1–16.
595 Blundy, J., and Wood, B. (1994) Prediction of crystal–melt partition coefficients from elastic
596 moduli. Nature, 372(6505), 452.

Blundy, J., and Wood, B. (2003) Mineral-melt partitioning of uranium, thorium and their daughters. Reviews in Mineralogy and Geochemistry, 52(1), 59-123.

Bourdon, B., and Sims, K. W. (2003) U-series constraints on intraplate basaltic magmatism. Reviews in Mineralogy and Geochemistry, 52(1), 215-254.

Cheng, H., Edwards, R. L., Shen, C. C., Polyak, V. J., Asmerom, Y., Woodhead, J., Hellstrom, J., Wang, Y., Kong, X., Spötl, C., and Wang, X. (2013) Improvements in ^{230}Th dating, ^{230}Th and ^{234}U half-life values, and U–Th isotopic measurements by multi-collector inductively coupled plasma mass spectrometry. Earth and Planetary Science Letters, 371, 82-91.

Cioni, R., Santacroce, R., and Sbrana, A. (1999) Pyroclastic deposits as a guide for reconstructing the multi-stage evolution of the Somma-Vesuvius Caldera. Bulletin of Volcanology, 61(4), 207-222.

Coble, M.A., Vazquez, J.A., Barth, A.P., Wooden, J., Burns, D., Kylander-Clark, A., Jackson, S., and Vennari, C.E. (2018) Trace element characterisation of MAD-559 zircon reference material for ion microprobe analysis. Geostandards and Geoanalytical Research, 42, 481-497.

Cortini, M., Ayuso, R. A., De Vivo, B., Holden, P., and Somma, R. (2004) Isotopic composition of Pb and Th in interplinian volcanics from Somma–Vesuvius volcano, Italy. Mineralogy and Petrology, 80(1-2), 83-96.

Crowley, J. L., and Schmitz, M. D. (2009) A precise comparison of U-Pb dates from baddeleyite and zircon: evidence for excess ^{207}Pb in baddeleyite. Eos, Transactions, American Geophysical Union 90(52):V53B-06.

Crowley, J. L., Schoene, B., and Bowring, S. A. (2007) U-Pb dating of zircon in the Bishop Tuff at the millennial scale. Geology, 35(12), 1123-1126.

620 Davidson, A., and Van Breemen, O. (1988) Baddeleyite-zircon relationships in coronitic
621 metagabbro, Grenville Province, Ontario: implications for geochronology. Contributions
622 to Mineralogy and Petrology, 100(3), 291-299.
623 Davis, W. J., and Davis, D. W. (2018) Alpha Recoil Loss of Pb from Baddeleyite Evaluated by
624 High-Resolution Ion Microprobe (SHRIMP II) Depth Profiling and Numerical Modeling:
625 Implications for the Interpretation of U-Pb Ages in Small Baddeleyite Crystals.
626 Microstructural Geochronology: Planetary Records Down to Atom Scale, 247-259.
627 Davies, J. H. F. L., Stern, R. A., Heaman, L. M., Moser, D. E., Walton, E. L., and Vennemann, T.
628 (2018) Evaluating baddeleyite oxygen isotope analysis by secondary ion mass
629 spectrometry (SIMS). Chemical Geology, 479, 113-122.
630 Di Renzo, V., Di Vito, M. A., Arienzo, I., Carandente, A., Civetta, L., D'antonio, M., Giordano,
631 F., Orsi, G., and Tonarini, S. (2007) Magmatic history of Somma–Vesuvius on the basis
632 of new geochemical and isotopic data from a deep borehole (Camaldoli della Torre).
633 Journal of Petrology, 48(4), 753-784.
634 Drake, M. J., and Weill, D. F. (1972) New rare earth element standards for electron microprobe
635 analysis. Chemical Geology, 10(2), 179-181.
636 Dunn, T., and Sen, C. (1994) Mineral/matrix partition coefficients for orthopyroxene,
637 plagioclase, and olivine in basaltic to andesitic systems: a combined analytical and
638 experimental study. Geochimica et Cosmochimica Acta, 58(2), 717-733.
639 Ernst, R. E., Buchan, K. L., and Campbell, I. H. (2005) Frontiers in large igneous province
640 research. Lithos, 79(3-4), 271-297.
641 Fahrig, W. F. (1987) The tectonic settings of continental mafic dyke swarms: Failed arm and
642 early passive margin: Geological Association of Canada Special Paper, 34, 331-348.

643 Fulignati, P., Marianelli, P., Santacroce, R., and Sbrana, A. (2004) Probing the Vesuvius magma
644 chamber–host rock interface through xenoliths. Geological Magazine, 141, 417-428.
645 Harley, S. L., and Kelly, N. M. (2007) The impact of zircon–garnet REE distribution data on the
646 interpretation of zircon U–Pb ages in complex high-grade terrains: an example from the
647 Rauer Islands, East Antarctica. Chemical Geology, 241(1-2), 62-87.
648 Harms, E., and Schmincke, H. U. (2000) Volatile composition of the phonolitic Laacher See
649 magma (12,900 yr BP): implications for syn-eruptive degassing of S, F, Cl and H_2O.
650 Contributions to Mineralogy and Petrology, 138(1), 84-98.
651 Harms, E., Gardner, J. E., and Schmincke, H. U. (2004) Phase equilibria of the Lower Laacher
652 See Tephra (East Eifel, Germany): constraints on pre-eruptive storage conditions of a
653 phonolitic magma reservoir. Journal of Volcanology and Geothermal Research, 134(1-2),
654 125-138.
655 Heaman, L. M. (2009) The application of U–Pb geochronology to mafic, ultramafic and alkaline
656 rocks: an evaluation of three mineral standards. Chemical Geology, 261(1-2), 43-52.
657 Heaman, L. M., and LeCheminant, A. N. (1993) Paragenesis and U-Pb systematics of baddeleyite
658 (ZrO_2). Chemical Geology, 110(1-3), 95-126.
659 Heaman, L. M., and LeCheminant, A. N. (2001) Anomalous U–Pb systematics in mantle-derived
660 baddeleyite xenocrysts from Ile Bizard: evidence for high temperature radon diffusion?
661 Chemical Geology, 172(1-2), 77-93.
662 Harms, E., Gardner, J. E., and Schmincke, H. U. (2004) Phase equilibria of the Lower Laacher
663 See Tephra (East Eifel, Germany): constraints on pre-eruptive storage conditions of a
664 phonolitic magma reservoir. Journal of Volcanology and Geothermal Research, 134(1-2),
665 125-138.

Herd, C. D. K., Simonetti, A., and Peterson, N. D. (2007) In situ U-Pb geochronology of Martian baddeleyite by laser ablation MC-ICP-MS. 38th Lunar and Planetary Science Conference, (Lunar and Planetary Science XXXVIII), held March 12-16, 2007 in League City, Texas. LPI Contribution No. 1338, p.1664.

Huang, F., Schmidt, M. W., Günther, D., and Eikenberg, J. (2009) Partitioning of protactinium, uranium, thorium and other trace elements between columbite and hydrous silicate melt. American Geophysical Union, Fall Meeting Abstracts, p. 2031.

Huang, F., Xu, J., and Zhang, J. (2016) U-series disequilibria in subduction zone lavas: Inherited from subducted slabs or produced by mantle in-growth melting? Chemical Geology, 440, 179-190.

Ibañez-Mejia, M., Gehrels, G. E., Ruiz, J., Vervoort, J. D., Eddy, M. E., and Li, C. (2014) Small-volume baddeleyite (ZrO_2) U–Pb geochronology and Lu–Hf isotope geochemistry by LA-ICP-MS. Techniques and applications. Chemical Geology, 384, 149–167.

Ickert, R. B., Mundil, R., Magee Jr, C. W., and Mulcahy, S. R. (2015) The U–Th–Pb systematics of zircon from the Bishop Tuff: a case study in challenges to high-precision Pb/U geochronology at the millennial scale. Geochimica et Cosmochimica Acta, 168, 88-110.

Jolis, E.M., Troll, V.R., Harris, C., Freda, C., Gaeta, M., Orsi, G., and Siebe, C. (2015) Skarn xenolith record crustal CO_2 liberation during Pompeii and Pollena eruptions, Vesuvius volcanic system, central Italy. Chemical Geology 415, 17–36.

Kato, Y., Yamaguchi, K. E., and Ohmoto, H. (2006) Rare earth elements in Precambrian banded iron formations: Secular changes of Ce and Eu anomalies and evolution of atmospheric oxygen. Evolution of Early Earth's Atmosphere, Hydrosphere, and Biosphere: Constraints from Ore Deposits, 198, 269.

689 Klemme, S., and Meyer, H. P. (2003) Trace element partitioning between baddeleyite and
690 carbonatite melt at high pressures and high temperatures. Chemical Geology, 199(3-4),
691 233-242.
692 LaTourrette, T., Hervig, R. L., and Holloway, J. R. (1995) Trace element partitioning between
693 amphibole, phlogopite, and basanite melt. Earth and Planetary Science Letters, 135(1-4),
694 13-30.
695 Marini, L., Chiappini, V., Cioni, R., Cortecci, G., Dinelli, E., Principe, C., and Ferrara, G. (1998)
696 Effect of degassing on sulfur contents and $\delta^{34}S$ values in Somma-Vesuvius magmas.
697 Bulletin of Volcanology, 60(3), 187-194.
698 McDonough, W. F., and Sun, S. S. (1995) The composition of the Earth. Chemical Geology,
699 120(3-4), 223-253.
700 Mitsuji, T. (1967) The Chemistry of Protactinium. IV. On the Absorption Spectra of Tetravalent
701 Protactinium in Aqueous Solutions. Bulletin of the Chemical Society of Japan, 40(9),
702 2091-2095.
703 Onuma, N., Higuchi, H., Wakita, H., and Nagasawa, H. (1968) Trace element partition between
704 two pyroxenes and the host lava. Earth and Planetary Science Letters, 5, 47-51.
705 Pappalardo, L., and Mastrolorenzo, G. (2010) Short residence times for alkaline Vesuvius
706 magmas in a multi-depth supply system, Evidence from geochemical and textural studies.
707 Earth and Planetary Science Letters 296, 133–143.
708 Pisarevsky, S. A., De Waele, B., Jones, S., Söderlund, U., and Ernst, R. E. (2015)
709 Paleomagnetism and U–Pb age of the 2.4 Ga Erayinia mafic dykes in the south-western
710 Yilgarn, Western Australia: Paleogeographic and geodynamic implications. Precambrian
711 Research, 259, 222-231.

712 Prytulak, J., Avanzinelli, R., Koetsier, G., Kreissig, K., Beier, C., and Elliott, T. (2014) Melting
713 versus contamination effects on ^{238}U–^{230}Th–^{226}Ra and ^{235}U–^{231}Pa disequilibria in lavas
714 from São Miguel, Azores. Chemical Geology, 381, 94-109.
715 Rasmussen, B., Fletcher, I. R., and Muhling, J. R. (2008) Pb/Pb geochronology, petrography and
716 chemistry of Zr-rich accessory minerals (zirconolite, tranquillityite and baddeleyite) in
717 mare basalt 10047. Geochimica et Cosmochimica Acta, 72(23), 5799-5818.
718 Reis, N. J., Teixeira, W., Hamilton, M. A., Bispo-Santos, F., Almeida, M. E., and D'Agrella-
719 Filho, M. S. (2013) Avanavero mafic magmatism, a late Paleoproterozoic LIP in the
720 Guiana Shield, Amazonian Craton: U–Pb ID-TIMS baddeleyite, geochemical and
721 paleomagnetic evidence. Lithos, 174, 175-195.
722 Reischmann, T. (1995) Precise U/Pb age determination with baddeleyite (ZrO_2), a case study
723 from the Phalaborwa igneous complex, South Africa. South African Journal of Geology,
724 98(1), 1-4.
725 Rioux, M., Bowring, S., Cheadle, M., and John, B. (2015) Evidence for initial excess ^{231}Pa in
726 mid-ocean ridge zircons. Chemical Geology, 397, 143-156.
727 Robert, J., Miranda, C. F., and Muxart, R. (1969) Mesure de la période du protactinium 231 par
728 microcalorimétrie. Radiochimica Acta, 11(2), 104-108.
729 Rolandi, G., Petrosino, P., and Mc Geehin, J. (1998) The interplinian activity at Somma–
730 Vesuvius in the last 3500 years. Journal of Volcanology and Geothermal Research, 82(1-
731 4), 19-52.
732 Scaillet, B., Pichavant, M., and Cioni, R. (2008) Upward migration of Vesuvius magma chamber
733 over the past 20,000 years. Nature 455, 216–219.

734 Scheibner, B., Heumann, A., Wörner, G., and Civetta, L. (2008) Crustal residence times of
735 explosive phonolite magmas: U–Th ages of magmatic Ca-Garnets of Mt. Somma-
736 Vesuvius (Italy). Earth and Planetary Science Letters, 276(3-4), 293-301.
737 Schmincke, H. U. (2007) The Quaternary volcanic fields of the east and west Eifel (Germany). In
738 J. R. R. Ritter and U.R. Christensen, Eds., Mantle Plumes - A Multidisciplinary
739 Approach, pp 241-322. Springer, Berlin, Heidelberg.
740 Schmitt, A. K. (2007) Ion microprobe analysis of (^{231}Pa)/(^{235}U) and an appraisal of protactinium
741 partitioning in igneous zircon. American Mineralogist, 92(4), 691-694.
742 Schmitt, A. K. (2011) Uranium series accessory crystal dating of magmatic processes. Annual
743 Review of Earth and Planetary Sciences, 39(1), 321-349.
744 Schmitt, A. K., Chamberlain, K. R., Swapp, S. M., and Harrison, T. M. (2010a) In situ U–Pb
745 dating of micro-baddeleyite by secondary ion mass spectrometry. Chemical Geology,
746 269(3-4), 386-395.
747 Schmitt, A. K., Wetzel, F., Cooper, K. M., Zou, H., and Wörner, G. (2010b) Magmatic longevity
748 of Laacher See Volcano (Eifel, Germany) indicated by U–Th dating of intrusive
749 carbonatites. Journal of Petrology, 51(5), 1053-1085.
750 Schmitz, M. D. and Bowring, S. A. (2001) U-Pb zircon and titanite systematics of the Fish
751 Canyon Tuff: an assessment of high-precision U-Pb geochronology and its application to
752 young volcanic rocks. Geochimica et Cosmochimica Acta, 65(15), 2571-2587.
753 Schuhmacher, M., de Chambost, E., McKeegan, K. D., Harrison, T. M., and Migeon, H. (1993)
754 In situ U/Pb dating of zircon with the CAMECA ims 1270. In A. Benninghoven, Y. Nihei,
755 R. Shimizu, H. W. Werner, Eds., Secondary Ion Mass Spectrometry SIMS IX: Chichester,
756 United Kingdom, Wiley, p. 919-922.

Sevink, J., van Bergen, M. J., Van Der Plicht, J., Feiken, H., Anastasia, C., and Huizinga, A. (2011) Robust date for the Bronze age Avellino eruption (Somma-Vesuvius): 3945±10 calBP (1995±10 calBC). Quaternary Science Reviews, 30(9-10), 1035-1046.

Shannon, R. D. (1976) Revised effective ionic radii and systematic studies of interatomic distances in halides and chalcogenides. Acta Crystallographica section A: crystal physics, diffraction, theoretical and general crystallography, 32(5), 751-767.

Smith, D. K., and Newkirk, W. (1965) The crystal structure of baddeleyite (monoclinic ZrO_2) and its relation to the polymorphism of ZrO_2. Acta Crystallographica, 18(6), 983-991.

Söderlund, U., Hofmann, A., Klausen, M. B., Olsson, J. R., Ernst, R. E., and Persson, P. O. (2010) Towards a complete magmatic barcode for the Zimbabwe craton: Baddeleyite U–Pb dating of regional dolerite dyke swarms and sill complexes. Precambrian Research, 183(3), 388-398.

Söderlund, U., Ibanez-Mejia, M., El Bahat, A., Ernst, R. E., Ikenne, M., Soulaimani, A., Youbi, N., Cousens, B., El Janati, M., and Hafid, A. (2013) Reply to Comment on "U–Pb baddeleyite ages and geochemistry of dolerite dykes in the Bas-Drâa inlier of the Anti-Atlas of Morocco: Newly identified 1380 Ma event in the West African Craton" by André Michard and Dominique Gasquet. Lithos, 174, 101-108.

Sulpizio, R., Cioni, R., Di Vito, M. A., Mele, D., Bonasia, R., and Dellino, P. (2010a) The Pomici di Avellino eruption of Somma-Vesuvius (3.9 ka BP). Part I: stratigraphy, compositional variability and eruptive dynamics. Bulletin of Volcanology, 72(5), 539-558.

Sulpizio, R., Bonasia, R., Dellino, P., Mele, D., Di Vito, M. A., and La Volpe, L. (2010b) The Pomici di Avellino eruption of Somma–Vesuvius (3.9 ka BP). Part II: sedimentology and

physical volcanology of pyroclastic density current deposits. Bulletin of Volcanology, 72(5), 559-577.

Teixeira, W., D'Agrella-Filho, M. S., Hamilton, M. A., Ernst, R. E., Girardi, V. A., Mazzucchelli, M., and Bettencourt, J. S. (2013) U–Pb (ID-TIMS) baddeleyite ages and paleomagnetism of 1.79 and 1.59 Ga tholeiitic dyke swarms, and position of the Rio de la Plata Craton within the Columbia supercontinent. Lithos, 174, 157-174.

Teixeira, W., Hamilton, M. A., Girardi, V. A., and Faleiros, F. M. (2016) Key Dolerite Dyke Swarms of Amazonia: U-Pb Constraints on Supercontinent Cycles and Geodynamic Connections with Global LIP Events Through Time. Acta Geologica Sinica-English Edition, 90, 84-85.

Tomlinson, E. L., Smith, V. C., Albert, P. G., Aydar, E., Civetta, L., Cioni, R., Çubukçu, E., Gertisser, R., Isaia, R., Menzies, M. A., Orsi, G., Rosi, M., and Zanchetta, G. (2015) The major and trace element glass compositions of the productive Mediterranean volcanic sources: tools for correlating distal tephra layers in and around Europe. Quaternary Science Reviews, 118, 48-66.

Turner, S., Regelous, M., Hawkesworth, C., and Rostami, K. (2006) Partial melting processes above subducting plates: constraints from ^{231}Pa–^{235}U disequilibria. Geochimica et Cosmochimica Acta, 70(2), 480-503.

van den Bogaard, P. (1995) $^{40}Ar/^{39}Ar$ ages of sanidine phenocrysts from Laacher See Tephra (12,900 yr BP): Chronostratigraphic and petrological significance. Earth and Planetary Science Letters, 133(1-2), 163-174.

Wendt, I., and Carl, C. (1985) U/Pb dating of discordant 0.1 Ma old secondary U minerals. Earth and Planetary Science Letters, 73(2-4), 278-284.

Wörner, G., and Schmincke, H. U. (1984) Petrogenesis of the zoned Laacher See tephra. Journal of Petrology, 25(4), 836-851.

Wiedenbeck, M. A. P. C., Alle, P., Corfu, F., Griffin, W. L., Meier, M., Oberli, F. V., Von Quadt, A., Roddick, J.C., and Spiegel, W. (1995) Three natural zircon standards for U-Th-Pb, Lu-Hf, trace element and REE analyses. Geostandards newsletter, 19(1), 1-23.

Wiedenbeck, M., Hanchar, J. M., Peck, W. H., Sylvester, P., Valley, J., Whitehouse, M., Kronz, A., Morishita, Y., Nasdala, L., Fiebig, J., and others (2004) Further characterisation of the 91500 zircon crystal. Geostandards and Geoanalytical Research, 28(1), 9-39.

Wood, B. J., and Blundy, J. D. (1997) A predictive model for rare earth element partitioning between clinopyroxene and anhydrous silicate melt. Contributions to Mineralogy and Petrology, 129(2-3), 166-181.

Wörner, G., Beusen, J. M., Duchateau, N., Gijbels, R., and Schmincke, H. U. (1983) Trace element abundances and mineral/melt distribution coefficients in phonolites from the Laacher See Volcano (Germany). Contributions to Mineralogy and Petrology, 84(2-3), 152-173.

Wu, W. N., Schmitt, A. K., and Pappalardo, L. (2015) U-Th baddeleyite geochronology and its significance to date the emplacement of silica undersaturated magmas. American Mineralogist, 100(10), 2082-2090.

Xie, L., Zhang, Y., Zhang, H., Sun, J., and Wu, F. (2008) In situ simultaneous determination of trace elements, U-Pb and Lu-Hf isotopes in zircon and baddeleyite. Chinese Science Bulletin, 53(10), 1565-1573.

List of figure captions

826 Figure 1. Evolution of $^{207}Pb/^{206}Pb$ deviations resulting from initial disequilibrium relative to Pb-
827 ingrowth under initial secular equilibrium conditions over the last 4.5 Ga. Curves were calculated
828 using equations from Wendt and Carl (1985) and initial D_{Pa}/D_U between 2 and 100 and D_{Th}/D_U =
829 1 (black). Once the curves intersect the hatched area (representing the analytical precision
830 routinely achieved with ID-TIMS), the effect of initial ^{231}Pa is smaller than the analytical
831 uncertainly, and thus becomes negligible. A model curve based on empirical baddeleyite-melt
832 partitioning ratios (D_{Pa}/D_U = 5 and D_{Th}/D_U = 0.01) is proposed as a realistic correction (red),
833 suggesting that ^{231}Pa excess significantly affects U/Pb baddeleyite ages for nearly the entire
834 Phanerozoic eon.

835 Figure 2. Optical and Scanning electron microscope images of the studied samples: (a)
836 Idiomorphic baddeleyite (Badd) crystals in interstitial volumes of sanidine (Sa). Optical image,
837 Vesuvius sample. (b) Optical image of the Laacher See syenite sample. (c) Euhedral hauyne (Hyn)
838 associated with sanidine (Sa) and opaque minerals (Op). Polished thin section under transmitted
839 light, Laacher See sample. (d) Clinopyroxene in Laacher See syenite, polished thin section under
840 transmitted light. (e)-(h) Representative backscattered electron (BSE) images of Vesuvius (e,f)
841 and Laacher See (g,h) baddeleyite, all grains polished and mounted in epoxy. Pcl = pyrochlore.
842 Red circles indicate spot locations of U-Th-Pa analyses by SIMS. Tiny bright spots are remnants
843 of the gold coating previously applied for SIMS.

844 Figure 3. Chondrite-normalized REE patterns obtained by SIMS: (a) Phalaborwa reference
845 baddeleyite, (b) Vesuvius baddeleyite, (c) Laacher See baddeleyite. Recommended CI chondrite
846 abundances by McDonough and Sun (1995) were used for normalization.

Figure 4. U/Th isochron diagrams for Vesuvius (a) and Laacher See baddeleyite (b) obtained by SIMS with ages calculated from isochron slopes using the ^{230}Th decay constant of Cheng et al. (2013). All uncertainties plotted and stated as 1σ.

Figure 5. Rank order plots showing measured (^{231}Pa)/(^{235}U) ratios in (a) Vesuvius and (b) Laacher baddeleyite samples. All uncertainties stated and plotted as 1σ.

Figure 6. Partition coefficient curves for trivalent (solid), tetravalent (dash) and pentavalent (dot dash) trace elements between Vesuvius baddeleyite and silicate melt (T = 1073 K) modelled using lattice strain theory and plotted against ionic radius. Ce is excluded from curve fitting due to its presence as both Ce^{3+} and Ce^{4+}. Parameters r_0 and E_0 for 5^+ cations were estimated as 0.8 Å and 1265 GPa, respectively. Best fit values for D_{Pa} estimated from the partition coefficient curves are 4.5 ± 0.5 (D_{Pa4+}) and 2500 +6250/-1900 (D_{Pa5+}) (uncertainties estimated from curve fitting using maximal and minimal values). For D_U, the estimated best fit values are 9 +1/-0.5 (D_{U4+}) and 3000 +7550/-2300 (D_{U5+}).

Figure 7. Partition coefficient curves for trivalent (solid), tetravalent (dash) and pentavalent (dot dash) trace elements between Laacher See baddeleyite and silicate melt (T = 1033 K) modelled using lattice strain theory and plotted against ionic radius. Ce is excluded from curve fitting due to its presence as both Ce^{3+} and Ce^{4+}. Parameters r_0 and E_0 for 5^+ cations were estimated as 0.8 Å and 982 GPa, respectively. Best fit values for D_{Pa} estimated from the partition coefficient curves are 4.9 ± 0.5 (D_{Pa4+}) and 480 +830/-330 (D_{Pa5+}) (uncertainties estimated from curve fitting using maximal and minimal values). For D_U, the best fit values are estimated as 8.0 +0.7/-0.5 (D_{U4+}) and 550 +980/-380 (D_{U5+}).

Tables

869 **Table 1**. Parameters of trivalent, tetravalent and pentavalent partition coefficient ($D_{baddeleyite\text{-}melt}$)
870 curves obtained by least square curve fitting. Uncertainties are reported as 1 standard errors of the
871 fits.

Sample	r_0 (Å)	±	D_0	±	E_0 (GPa)	±
			Trivalent cations (3^+)			
Vesuvius	0.951	0.013	0.26	0.087	1 040	417
Laacher See	0.899	0.005	70.5	17.8	1206	163
			Tetravalent cations (4^+)			
Vesuvius	0.832	0.001	8203	1777	1265	79.3
Laacher See	0.831	0.001	1692	143	982	16.2
			Pentavalent cations (5^+)			
Vesuvius	0.8*	-	5981	+15150/-4596[1]	1265*	-
Laacher See	0.8*	-	945	+3575/-653[1]	982*	-

872 **Notes.** *parameter set as fixed value, [1]uncertainties estimated from curve fitting using maximal and
873 minimal data point.

874

Figure 1

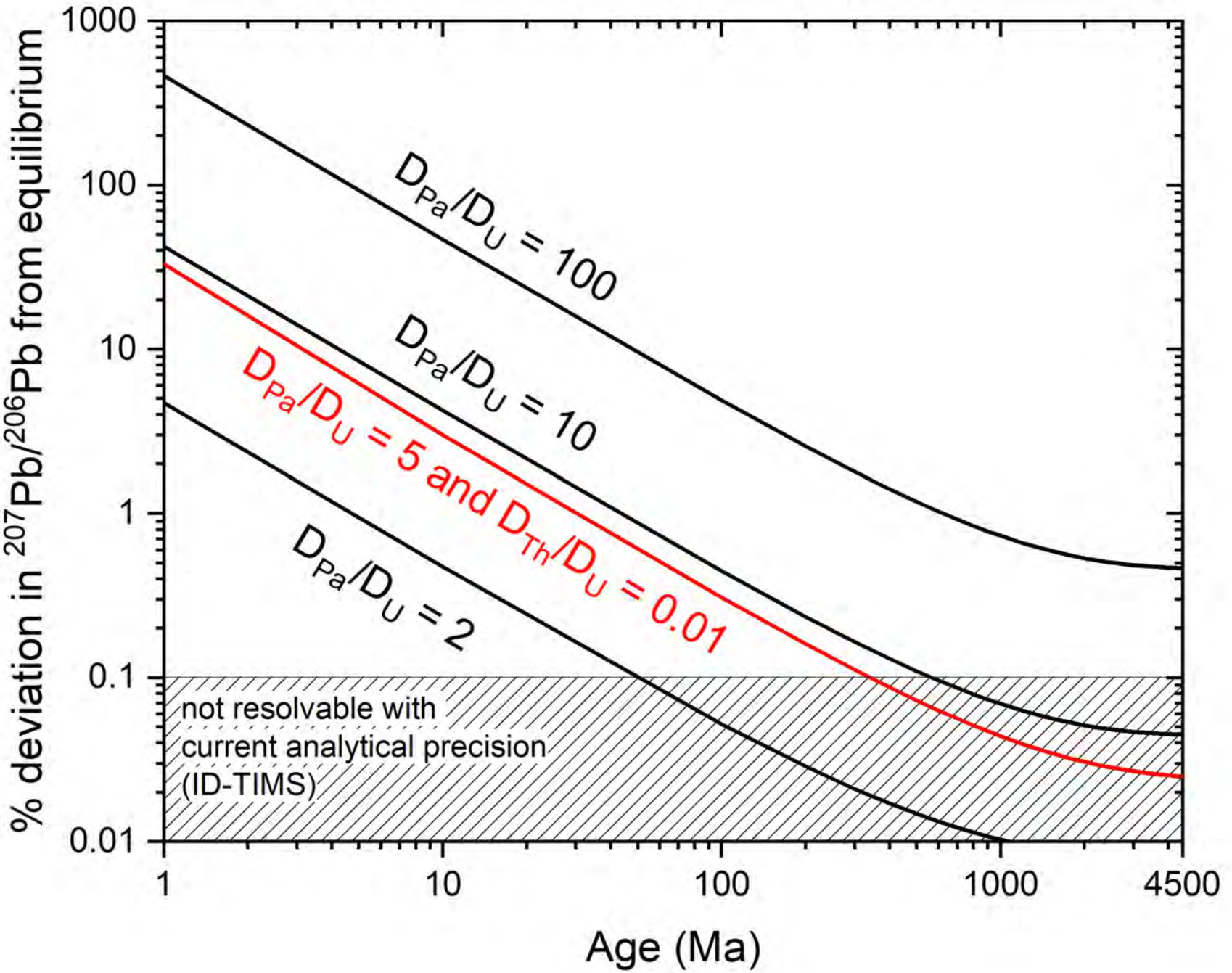
% deviation in $^{207}Pb/^{206}Pb$ from equilibrium
1000
100
10
1
0.1
0.01
1
10
100
1000
4500
Age (Ma)
D_{Pa}/D_U = 100
D_{Pa}/D_U = 10
D_{Pa}/D_U = 5 and D_{Th}/D_U = 0.01
D_{Pa}/D_U = 2
not resolvable with
current analytical precision
(ID-TIMS)

Figure 2

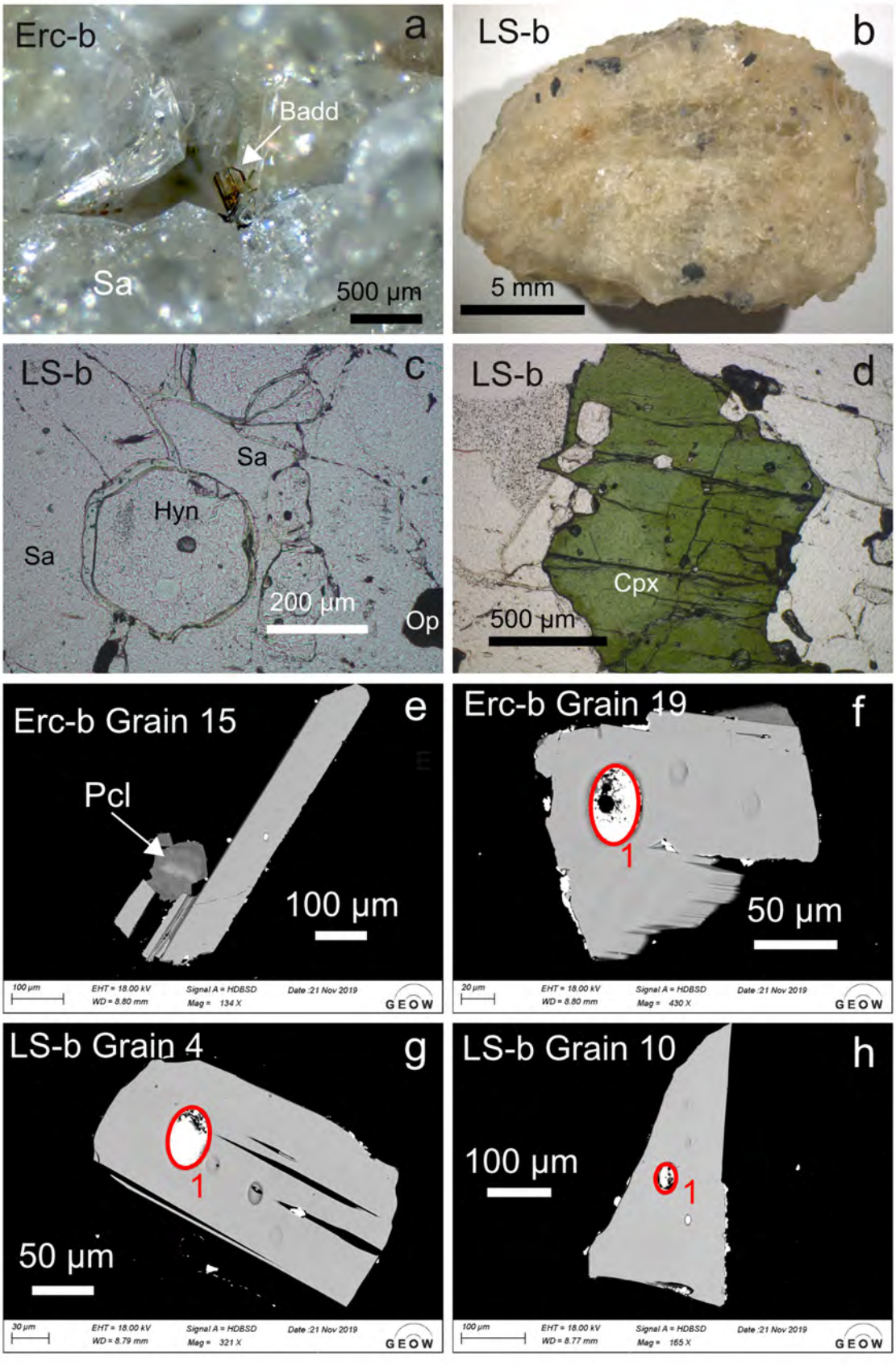
Erc-b
a
Badd
Sa
500 µm
LS-b
b
5 mm
LS-b
c
Sa
Hyn
Sa
200 µm
Op
LS-b
d
Cpx
500 µm
Erc-b Grain 15
e
Pcl
100 µm
100 µm EHT = 18.00 kV WD = 8.80 mm Signal A = HDBSD Mag = 134 X Date :21 Nov 2019 GEOW
Erc-b Grain 19
f
1
50 µm
20 µm EHT = 18.00 kV WD = 8.80 mm Signal A = HDBSD Mag = 430 X Date :21 Nov 2019 GEOW
LS-b Grain 4
g
1
50 µm
30 µm EHT = 18.00 kV WD = 8.79 mm Signal A = HDBSD Mag = 321 X Date :21 Nov 2019 GEOW
LS-b Grain 10
h
100 µm
1
100 µm EHT = 18.00 kV WD = 8.77 mm Signal A = HDBSD Mag = 165 X Date :21 Nov 2019 GEOW

Figure 3

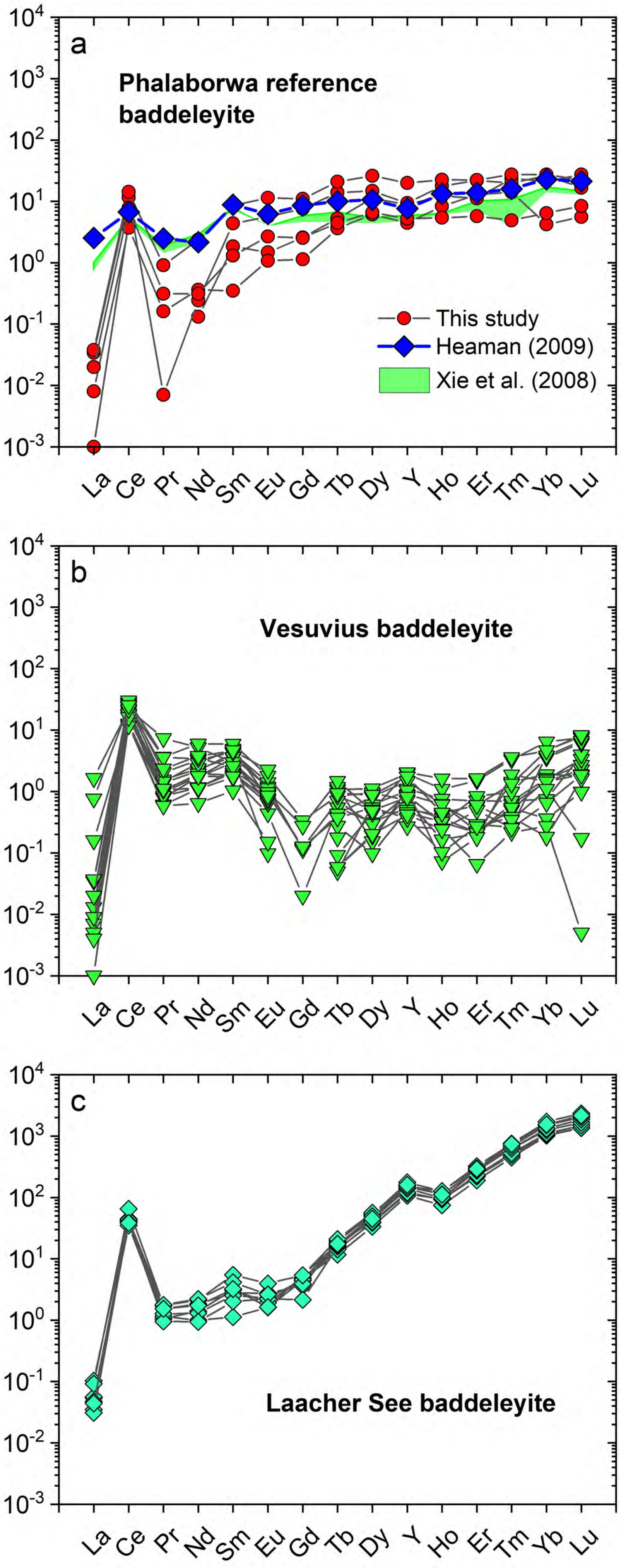
a
Phalaborwa reference baddeleyite
This study
Heaman (2009)
Xie et al. (2008)
b
Vesuvius baddeleyite
c
Laacher See baddeleyite
10^4
10^3
10^2
10^1
10^0
10^{-1}
10^{-2}
10^{-3}
La Ce Pr Nd Sm Eu Gd Tb Dy Y Ho Er Tm Yb Lu

Figure 4

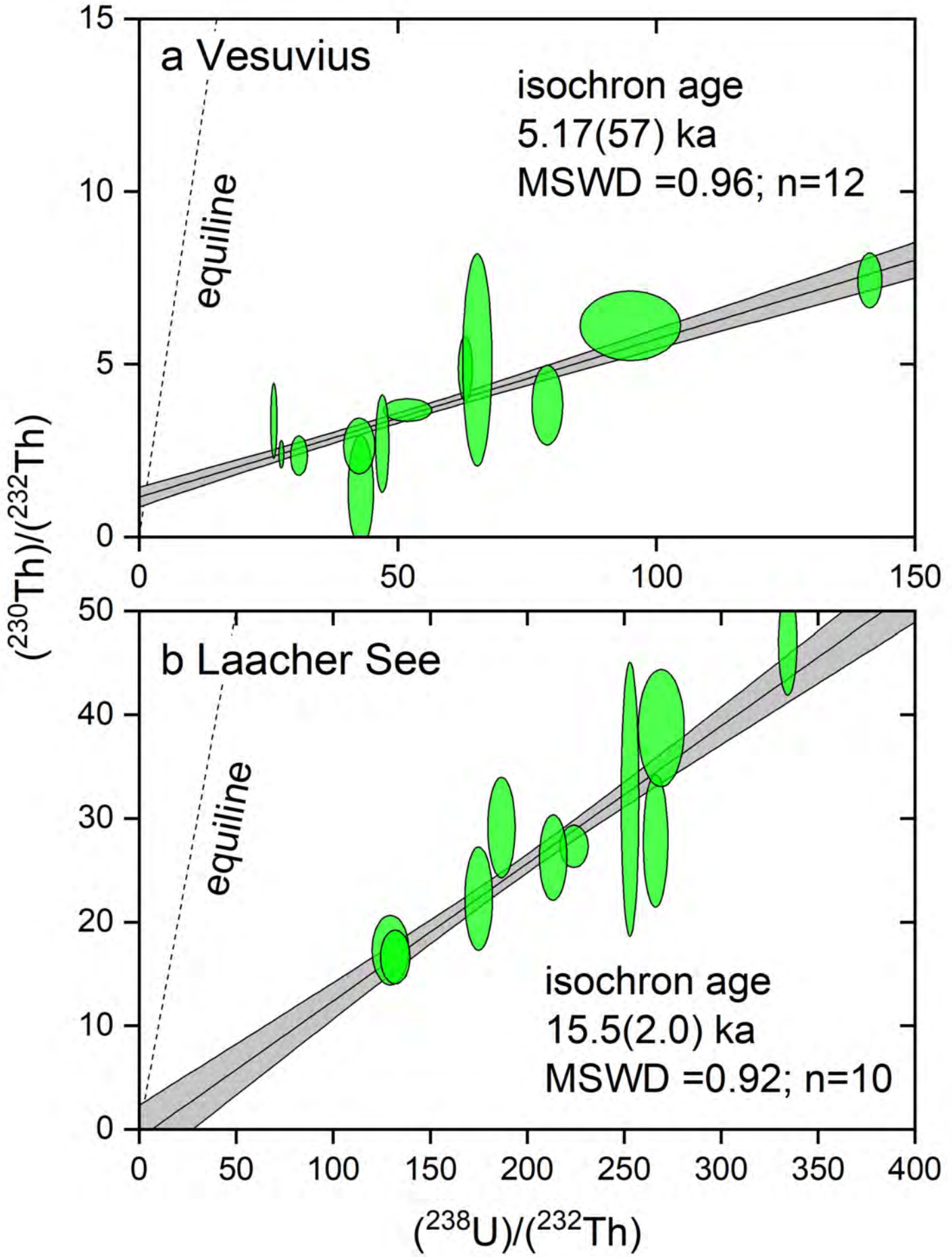
a Vesuvius
isochron age
5.17(57) ka
MSWD =0.96; n=12
equiline
b Laacher See
isochron age
15.5(2.0) ka
MSWD =0.92; n=10
equiline
(230Th)/(232Th)
(238U)/(232Th)
0
5
10
15
0
50
100
150
0
10
20
30
40
50
0
50
100
150
200
250
300
350
400

Figure 5

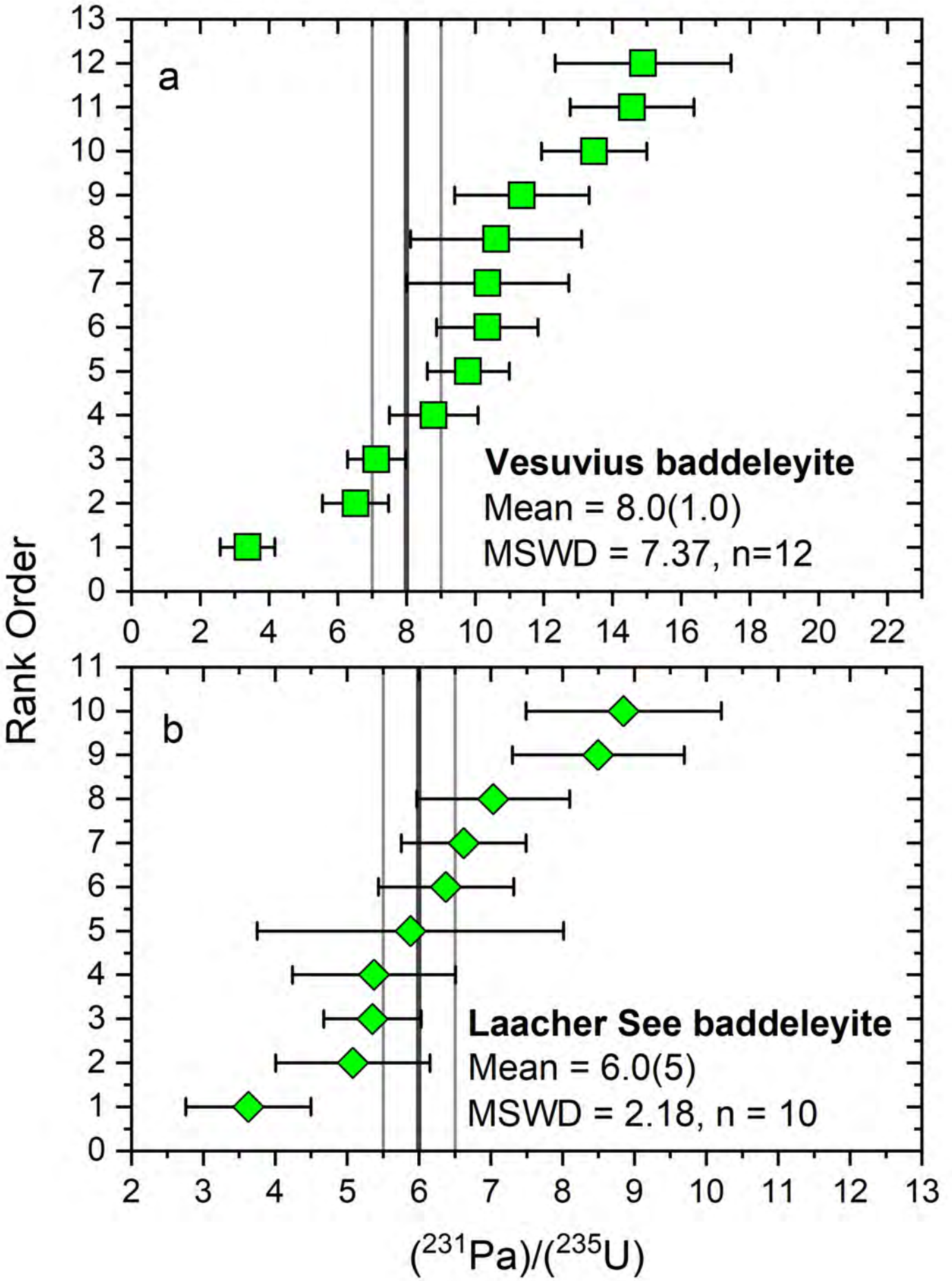
a
Vesuvius baddeleyite
Mean = 8.0(1.0)
MSWD = 7.37, n=12
b
Laacher See baddeleyite
Mean = 6.0(5)
MSWD = 2.18, n = 10
Rank Order
(231Pa)/(235U)

Figure 6

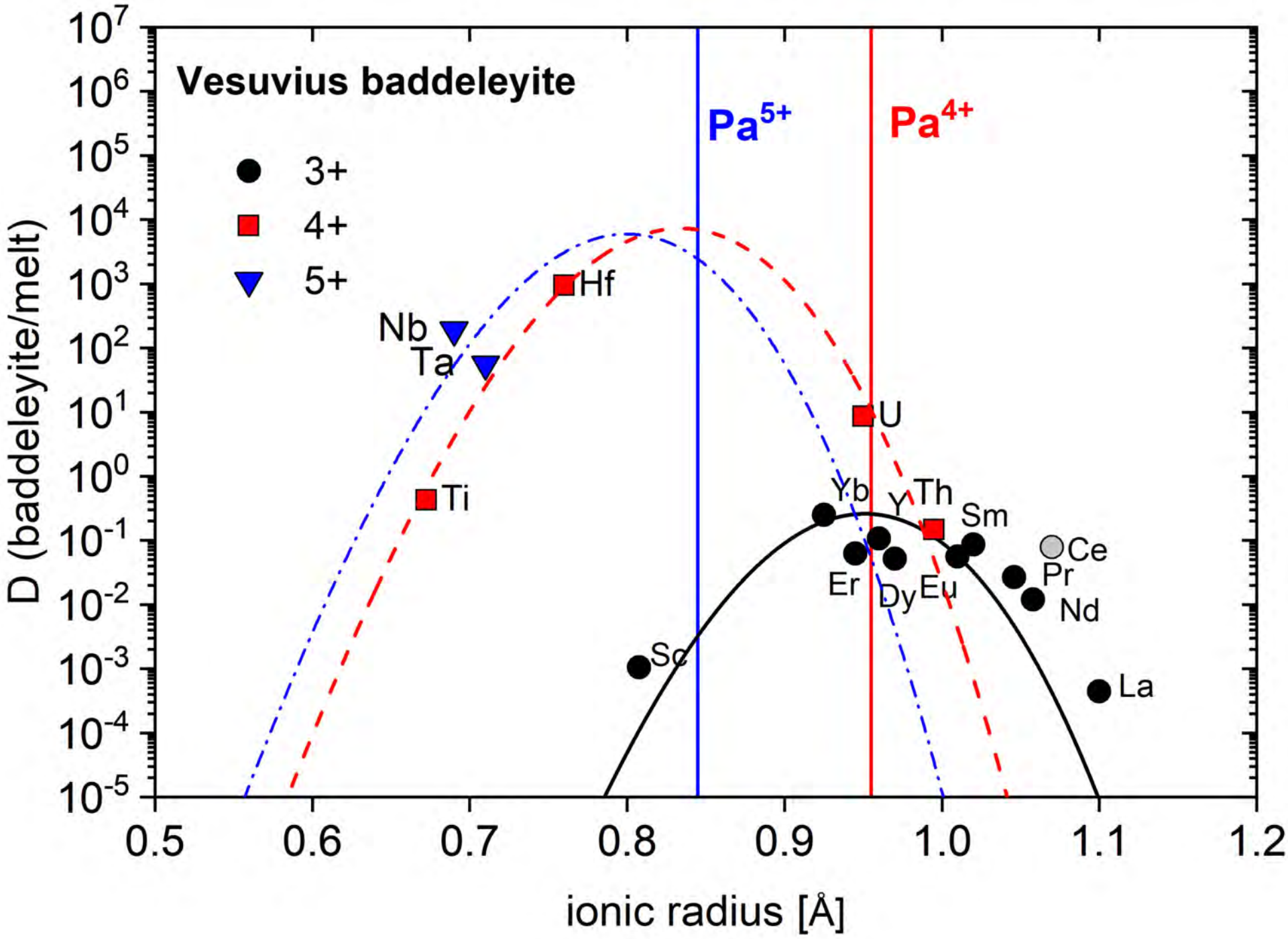
Vesuvius baddeleyite
3+
4+
5+
Pa5+
Pa4+
Hf
Nb
Ta
Ti
U
Yb
Y
Th
Sm
Ce
Pr
Nd
Er
Dy
Eu
Sc
La
D (baddeleyite/melt)
ionic radius [Å]
10^7
10^6
10^5
10^4
10^3
10^2
10^1
10^0
10^-1
10^-2
10^-3
10^-4
10^-5
0.5
0.6
0.7
0.8
0.9
1.0
1.1
1.2

Figure 7

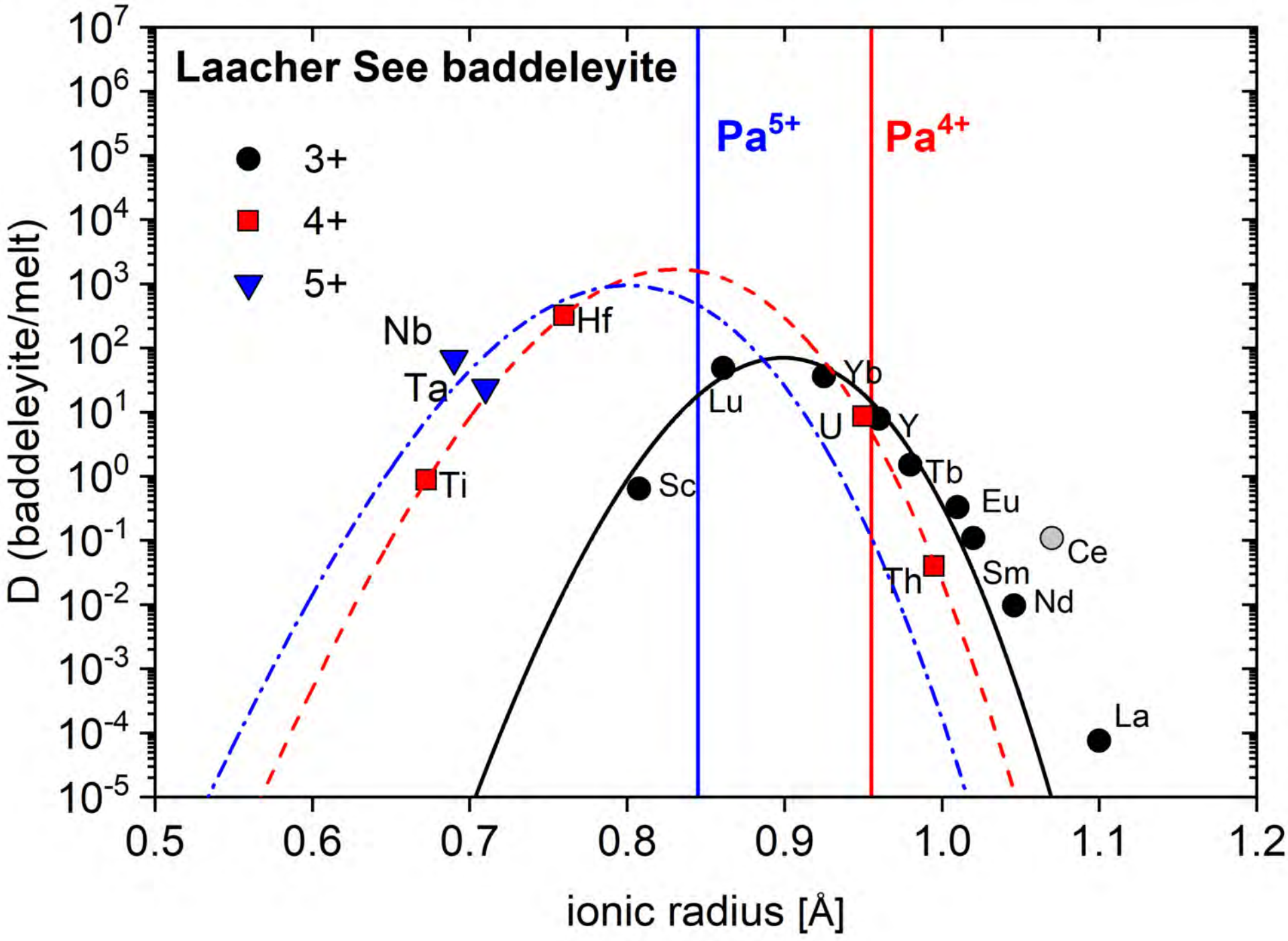
Laacher See baddeleyite
3+
4+
5+
Pa5+
Pa4+
Nb
Ta
Hf
Ti
Sc
Lu
Yb
U
Y
Tb
Eu
Ce
Sm
Th
Nd
La
D (baddeleyite/melt)
ionic radius [Å]
10^7
10^6
10^5
10^4
10^3
10^2
10^1
10^0
10^-1
10^-2
10^-3
10^-4
10^-5
0.5
0.6
0.7
0.8
0.9
1.0
1.1
1.2